IOP Publishing Physica Scripta
Phys. Scr. 95 (2020) 055215 (22pp) https://doi.org/10.1088/1402-4896/ab6e4c

A self-sustained oscillator to the Lorenz-Haken dynamics

Belkacem Meziane

Univ. Artois, CNRS, Centrale Lille, ENSCL, Univ. Lille, UMR 8181 – UCCS – Unité de Catalyse et Chimie du Solide, F-62300 Lens, France

E-mail: belkacem.meziane@univ-artois.fr

Received 17 September 2019, revised 14 January 2020
Accepted for publication 21 January 2020
Published 2 March 2020

Abstract

An operative transformation of the 3D Lorenz-Haken model into an exclusive second-order differential equation is proposed. The periodic solutions highlighting the original set forthrightly generate with the basic analytical tools and procedures of a one-dimensional forced oscillator, as that of a mass-spring system experiencing external harmonic-excitation. Evidencing with the oscillator structure, the inherent nonlinear dynamics interprets in terms of a resonant singularity rooted in the original 3D system. Appropriate analyses consistently adjust to the small and strong harmonic signals, supplying crucial formulations to ascertain the solution characteristics with the ultimate goal to describe, analytically, periodic phase-space trajectories.

Keywords: Lorenz equations, laser theory, instabilities and chaos, nonlinear dynamics, fluid turbulence, Chaos

(Some figures may appear in colour only in the online journal)

1. Introduction

After more than half-a-century of sustained investigations, the Lorenz-Haken equations, known to deliver a wealth of solutions, extending from ordered periodic trajectories to chaotic attractors, remain a subject filled with yet to unravel complexities [1–11]. The one way to pull out any information with respect to the system's transient and permanent output signals is to call for numerical analysis. However, in terms of the physics underlining the quite capricious behavior, no simple scheme is easy to capture and to put forward with mere digital results, thus leaving to reckless nonlinear interactions full accountability of the quite-often unpredictable behavior. As a challenge to elucidate a few ambiguities they carry, we aim at transforming the three nonlinearly coupled first-order differential equations into a single second-order structure for the population inversion. The electric field and intensity variations acting as the main excitation mechanisms competing to force the system into small or high-amplitude oscillations, contingent to the exact initial conditions and control parameter values the system submits-to.

After exposing the main steps of the conversion procedure, we shall analyze the non-linear oscillator in both the small and strong-harmonic regimes, extracting first-hand and useful analytical information. In particular, we shall derive two expressions that perfectly quantify the phase difference between the electric field and population inversion, when these develop in the vicinity or away from steady state. Such new outcomes will enable trustful reconstitutions of typical closed loops with well-ordered orbits, perfectly matching those simulated with the original 3D set.

Even though much of the report gravitates around Laser physics, the mathematical outcomes extend to the general issue of applied mathematics. Worth reminding is that, in 1998, Stephen Smale, the 1966, medal-Field laureate included the Lorenz equations-originally derived to deal with dissipative hydrodynamic flows [1]- in a list of 18 mathematical problems to challenge the 21st century [5]. The oscillator approach shines enough light to answer a few questions to Smale concerns and reactivate a subject left on a stand-by mathematical-mode by the scientific community, computers having taken the lead, without cracking the attractor mystery.

The presentation organizes according to the following hierarchy. The structuring procedure and basic algebra provide in section 2. Section 3 focuses on the small harmonic case, for which the phase space portraits consist of single-branch loops conforming to the regular oscillations that take place around steady state. Analytical descriptions of

these trajectories relate to the derivation of a phase factor that quantifies the time lag between the electric field and population inversion along with the associated amplitude response, exclusively relating to the control parameters. Some resonant phenomenon identifies to characterize the population response with respect to the cavity decay rate. Section 4 follows to focus on the strong harmonic mode, analytical reconstitutions of the phase-space double-branch trajectories as a primary goal to accomplish. Likewise, some characteristic phase factor and amplitude curves construct analytically to adequately follow those of the numerical solutions. Section 5 points out auxiliary notes, bringing to attention the driving role of the population inversion on the electric-field dynamics. Section 6 concludes with a few remarks pertaining to yet to explore aspects. Finally, four appendixes devote to detailing the primary steps to smooth-out some of the lengthy algebra, and a fifth one to recall, with some compulsory details, the main properties of the forced mass-spring harmonic oscillator. Its understanding points-out as a fundamental prerequisite for the newly proposed model to take hold of the complex Lorenz-Haken dynamics and main specifics. For that reason, reading appendix D first is highly recommended!

2. The structuring procedure

Using Newton's notation for time derivatives, the Lorenz-Haken equations write [7, 12]

$$\dot{E}(t) = -\kappa(E(t) + 2CP(t)), \tag{1a}$$

$$\dot{P}(t) = -P(t) + E(t)D(t), \tag{1b}$$

$$\dot{D}(t) = -\gamma(D(t) + 1 + E(t)P(t)). \tag{1c}$$

Where $E(t)$, $P(t)$, and $D(t)$ represent, respectively, the laser field amplitude, the polarization, and the population inversion of the amplifying medium. κ and γ are the field and population relaxation rates, both scaled to the polarization decay rate, while 2 C quantifies some external power supply, meant to break the natural thermodynamic equilibrium and transform an initially absorbing material into an amplifier. The dot above all three variables represents the first derivative with respect to time.

The key clue to the conversion method consists in reordering equation (1*a*) as

$$P(t) = -\frac{1}{2C}\left(E(t) + \frac{\dot{E}(t)}{\kappa}\right), \tag{2a}$$

transforming equation (1*b*) into

$$\dot{P}(t) = \frac{E(t)}{2C} + \frac{\dot{E}(t)}{2C\kappa} + E(t)D(t). \tag{2b}$$

Equation (1*c*) second derivative follows

$$\ddot{D}(t) = -\gamma\dot{D}(t) - \gamma\dot{E}(t)P(t) - \gamma E(t)\dot{P}(t) \tag{2c}$$

Subsequent to elementary transformations, equations (2*a*) and (2*b*) inject into equation (2*c*) to end-up with

$$\frac{1}{\gamma}\ddot{D}(t) + \dot{D}(t) + E(t)^2D(t) = \frac{1}{2C}\left(E(t)\dot{E}(t)\left(1 - \frac{1}{\kappa}\right) + \frac{\dot{E}(t)^2}{\kappa} - E(t)^2\right) \tag{3a}$$

or, equivalently

$$\frac{1}{\gamma}\ddot{D}(t) + \dot{D}(t) + E(t)^2D(t) = \frac{1}{2C}\left(\frac{E(t)^2}{2}\left(1 - \frac{1}{\kappa}\right) + \frac{\dot{E}(t)^2}{\kappa} - E(t)^2\right) \tag{3b}$$

This last equation specifies the dynamics of light-matter interactions to point out that, as the driving forces, the field intensity and its derivative implicate with competing influences. While the electric-field intensity-impact is to lessen the population inversion, its derivative has the inverse effect to enhancing it.

In view of its simple structure, one is entitled to wonder whether equations (3*a*) or (3*b*) is not contained inside any of the contributions –counting in hundreds, if not thousands– that dealt with the Lorenz-Haken equations since the first papers, from the early 1960's, for Lorenz [1,] to the mid 1970's, for Haken [2]. To the best of our knowledge, this is its first coming out in a report devoted to the basic example of nonlinear dynamics. If no author proposed such a structure, thus far, it is almost certainly because none thought of the clue to transforming equation (1*a*) into equation (2*a*). The conversion to a second-order differential equation is quite easy, yet impossible to carry out, in the oscillator form, without such a hint.

For fundamental and straightforward comparisons, let us recall the well-known mass-spring oscillator and basic theory [see appendix D for detailed reminders]. Subject to an external harmonic force, its motion along some x axis describes with the typical second-order differential equation

$$\ddot{x}(t) + \alpha\dot{x}(t) + \omega_0^2 x(t) = \mathrm{a}\cos(\omega t). \tag{4a}$$

The solution, which monitors the instantaneous mass position, follows

$$x(t) = A(\omega)\cos(\omega t + \varphi(\omega)). \tag{4b}$$

Amplitude $A(\omega)$ and phase $\varphi(\omega)$ pull out through direct plugging equation (4*b*) into equation (4*a*).

Equation (3*b*) bears some formal similarity with the one-dimensional forced oscillator, the population inversion as the equivalent of the mass-spring system, whereas the field intensity and derivatives play the roles of two competing driving forces. Equation (3*b*), right-hand side, clearly indicates that while the field intensity, with its negative sign, tends, as expected, to reduce the population inversion; on the contrary, both the field and intensity variations, with their

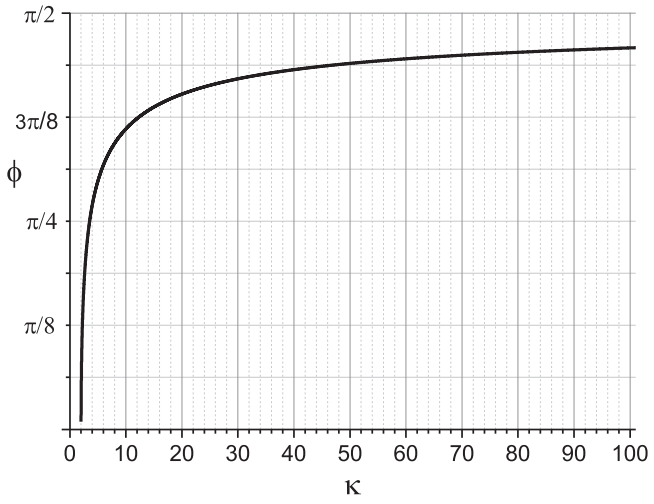

Figure 1. Electric field and population phase-mismatch with respect to the cavity decay-rate κ.

positive signs, incline to increasing it. Let us also note that light-matter interactions fully act through the product $E(t)^2D(t)$, which couples the laser intensity to the population inversion.

In addition, let us recall that, at the atomic level, during its transitions between low and high energy levels, an inverted atom has all the characteristics of a forced harmonic oscillator interacting with an electromagnetic field. It describes with a theoretical model identical to equation (4*a*). Therefore, it should be of no surprise to retrieve, at the macroscopic level, the equation of a forced oscillator with some higher level of complexity, bound to unravel in the coming sections.

Indeed, just as in the case of the forced mass-spring oscillator, we need some initial expression for the driving electric field in order to inspect the population inversion response and characteristics. Leaning on the solution features of the 3D system, as numerically simulated with adapted algorithms, the following sections successively deal with the small and strong-harmonic modes.

3. The small-harmonic mode

To draw straightforward similarities with the dynamic characteristics of the mass-spring system, we shall first derive an analytical expression of the phase mismatch between the exciting variable (the electric field) and the population response, with respect to the cavity decay rate. A few analytical solutions will follow, calling for phase mismatch evaluation, before focusing on the oscillator resonant properties, validating a one to one similarity between the population dynamics and any oscillator undergoing external excitation with varying frequency.

3.1. Phase mismatch factor

We know, from numerical analysis, that the Lorenz equations possess both soft harmonic and more complex solutions of the strong amplitude type. Aside from mere computing, analytical modelling may achieve with high-order harmonic-expansions, in the case of regular pulse structuring and subharmonic cascading [7, 12, 13], which take place when the initial conditions are strong enough to shift the system away from its stable state with growing amplitude oscillations.

For small enough perturbations, the electric field signal consists of small amplitude undulations around steady state, describing as

$$E(t) = E_0 + e\cos(\omega t) \tag{5}$$

With $e \ll E_0$.

Neglecting second order terms in e, equations (3*a*) and (3*b*) rewrite

$$\frac{1}{\gamma}\ddot{D}(t) + \dot{D}(t) + (E_0^2 + 2eE_0\cos(\omega t))D(t) \cong \frac{1}{2C}\left(-e\omega E_0\sin(\omega t)\left(1 - \frac{1}{\kappa}\right) - E_0^2 - 2eE_0\cos(\omega t)\right), \tag{6a}$$

indicative of a driving force

$$f(t) = f_0 + f_1\cos(\omega t) + f_2\sin(\omega t), \tag{6b}$$

The population response is bound to follow a similar expansion

$$D(t) = D_0 + d_1\cos(\omega t) + d_2\sin(\omega t) \tag{6c}$$

With straightforward algebra (see appendix A for details), equation (6a) yields

$$d_1 = \frac{\omega^2}{\left(\frac{\omega^2}{\gamma} - E_0^2\right)^2 + \omega^2}\frac{1}{2C}eE_0\left(1 - \frac{1}{\kappa}\right) \tag{6d}$$

$$d_2 = \frac{\omega\left(\frac{\omega^2}{\gamma} - E_0^2\right)}{\left(\frac{\omega^2}{\gamma} - E_0^2\right)^2 + \omega^2}\frac{1}{2C}eE_0\left(1 - \frac{1}{\kappa}\right). \tag{6e}$$

At the instability threshold, we know from linear stability analysis [7] that the steady state intensity E_0^2 and pulsation $\omega = \omega_0$ relate to the control parameters κ and γ, to fulfill the following expressions

$$E_0^2 = 2C - 1 = \frac{(\kappa + 1)(\kappa + 1 + \gamma)}{\kappa - 1 - \gamma}, \tag{7a}$$

$$\omega_0^2 = \frac{2\kappa\gamma(\kappa + 1)}{\kappa - 1 - \gamma} \tag{7b}$$

Both combining to yield

$$\frac{\omega_0^2}{\gamma} - E_0^2 = \frac{2(+1)}{\kappa - 1 - \gamma} - \frac{(\kappa + 1)(\kappa + 1 + \gamma)}{\kappa - 1 - \gamma} = \kappa + 1 \tag{7c}$$

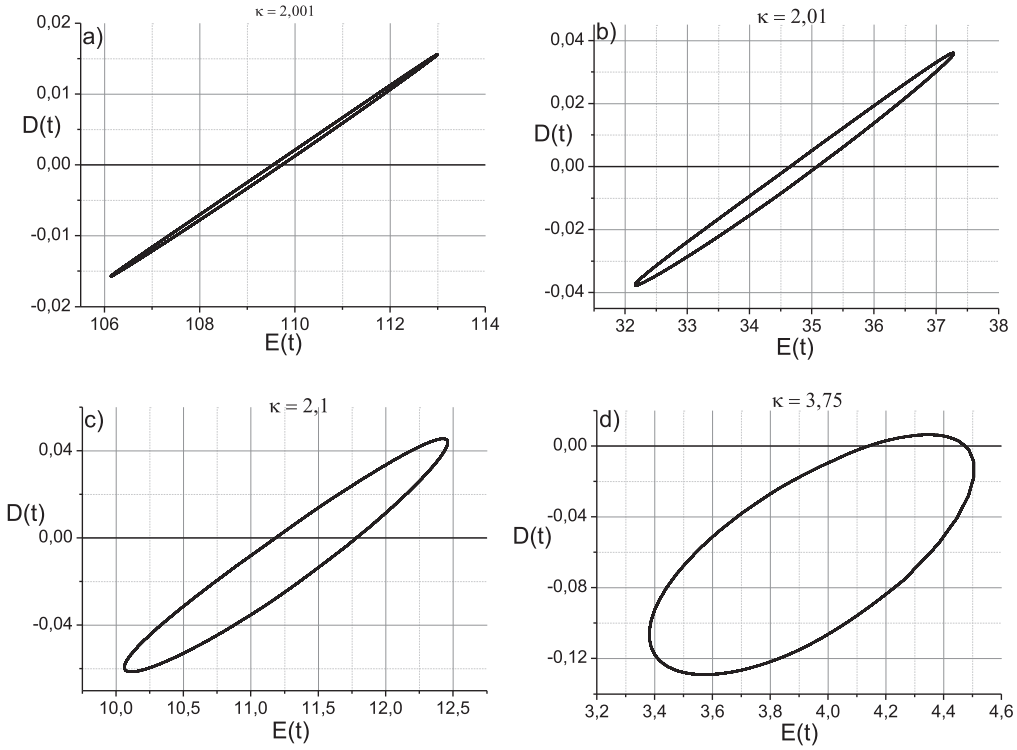

Figure 2. Phase-space limit cycles, numerically simulated with equation (1); (a) $\kappa = 2.001$, (b) $\kappa = 2.01$, (c) $\kappa = 2.1$, and (d) $\kappa = 3.75$.

From equations (6*c*), (6*d*) and (7*c*), we pull out a relationship between the in-phase and out-of-phase population components, which simplifies into

$$\frac{d_2}{d_1} = \sqrt{\frac{(\kappa + 1)(\kappa - 1 - \gamma)}{2\kappa\gamma}} \tag{8}$$

This ratio represents an important information pertaining to the phase difference between the electric field and population inversion oscillations. In fact, with no phase difference, each variable is bound to converge towards its stable state.

The population harmonic-components rearranging as

$$d_1 \cos(\omega t) + d_2 \sin(\omega t) = d_0 \cos(\omega t - \varphi), \tag{9a}$$

we deduce an expression for $\tan(\varphi)$ with an exclusive dependence on κ and γ

$$\tan(\varphi) = \frac{d_2}{d_1} = \sqrt{\frac{(\kappa + 1)(\kappa - 1 - \gamma)}{2\kappa\gamma}}, \tag{9b}$$

from which, we infer $\varphi(\kappa) = 0$, for $\kappa = 1 + \gamma$, and an asymptotic value $\varphi(\kappa) \to \frac{\pi}{2}$, when $\kappa \to \infty$.

At this point, it is worth emphasizing on the main differences between the forced mass-spring system and the self-sustained oscillator. Under some harmonic force, the mechanical oscillator response (or its equivalent electrical) follows that of the external excitation. Once the mass and spring characteristics are fixed, the amplitude and phase of the mass motion relate exclusively to the excitation pulsation it undergoes, eventually concluding in the well-known resonance phenomenon for some characteristic pulsation ω_0 [see appendix D for full tutorial]. On the other hand, the nonlinear laser oscillator drives with a constant external excitation 2 *C*, its behavior being contingent to the cavity and decay rates κ and γ. Beyond the instability threshold, and under bad-cavity conditions ($\kappa > \gamma$), the interacting electric-field and population-inversion compete and start to oscillate with a frequency $f_0 = \frac{1}{2\pi}\sqrt{\frac{2\kappa\gamma(\kappa+1)}{\kappa-1-\gamma}}$, and a phase difference $\varphi = \text{a tan}\left(\sqrt{\frac{(\kappa+1)(\kappa-1-\gamma)}{2\kappa\gamma}}\right)$, with exclusive dependency on κ and γ. In other words, when instability sets in, the cavity and population decay rates play, implicitly, the same role as the external driving pulsation of a mass-spring oscillator.

Figure 1 represents $\varphi(\kappa)$, for $\gamma = 1$. The graph shows rapidly increasing values for small κ's and much slower growth converging towards $\frac{\pi}{2}$, in the higher region.

3.2. Analytical solutions

In order to check for the extent of validity of these first elements, let us focus on a few harmonic solutions, numerically obtained from equation (1). Represented in a $D(t)$-versus-$E(t)$ phase-space axes, figure 2 shows four examples of limit cycles that correspond to a sequence of arbitrarily chosen κ values, indicated in the figure caption.

To match the examples of figure 2, the phase values compute from equation (9*b*) as (a) $\kappa = 2.001$, $\varphi \cong \frac{\pi}{100}$; (b) $\kappa = 2.01$, $\varphi \cong \frac{\pi}{36}$; (c) $\kappa = 2.1$, $\varphi \cong \frac{\pi}{12}$; and (c) $\kappa = 3.75$, $\varphi \cong \frac{\pi}{4}$.

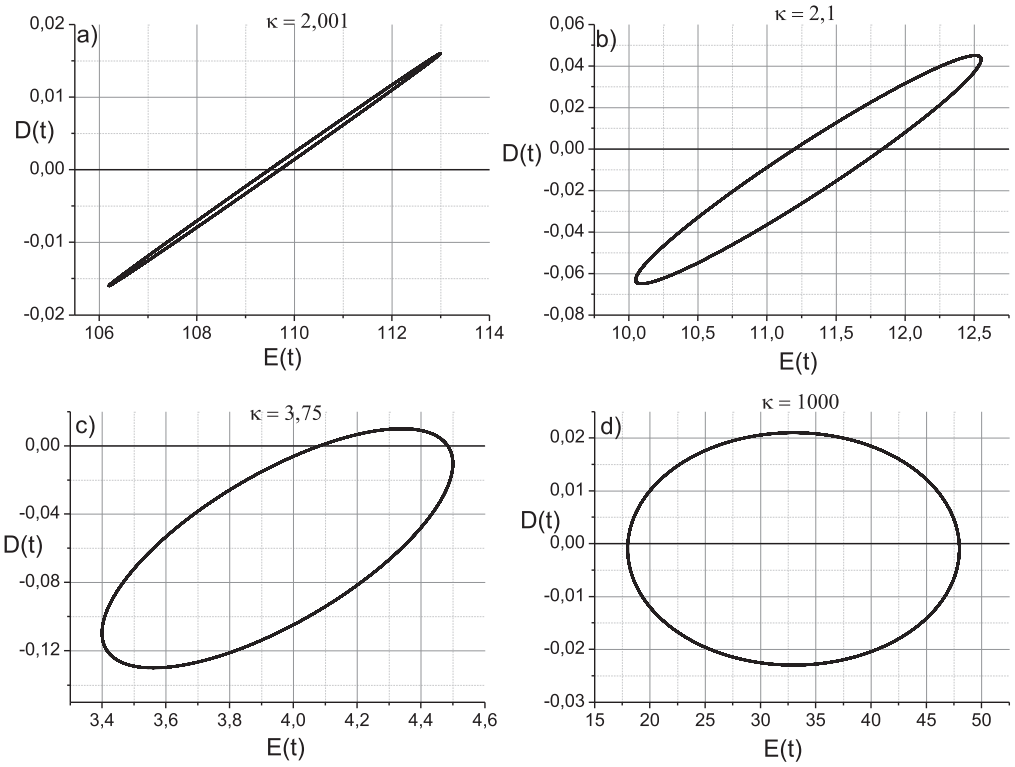

Figure 3. Analytical orbits obtained with equations (10*a*) and (10*b*), and the numerical coefficients of table 1. Note the perfect correspondence with the numerically simulated counterparts of figure 2. Also note the symmetrical elliptic orbit obtained with the asymptotic constants $\kappa = 1000$ and $\varphi = \frac{\pi}{2}$.

According to equations (5), (6*c*) and (9*a*), soft harmonic solutions should follow

$$E(t) = E_0 + e\cos(\omega t), \tag{10a}$$

for the electric field, and

$$D(t) = D_0 + d_0\cos(\omega t - \varphi), \tag{10b}$$

for the population inversion.

Given the electric field and population steady-states values, along with the perturbation strength e and associated amplitude d_0, the numerical orbits of figure 2 reproduce with exact similarities.

To cover the prospects to asymptotic κ values, the phase-space loops of figure 3 extend from (a) $\kappa = 2.001$, (b) $\kappa = 2.1$, (c) $\kappa = 3.75$, to (d) $\kappa = 1000$. All related coefficients gather in table 1.

Close inspections and comparisons between the graphs of figures 2 and 3 are persuasive enough to endorse the second-order self-sustained model of the Lorenz equations, inside the whole control parameter domain, as long as initial conditions sustain soft harmonic solutions.

3.3. Resonant characteristics in the small-harmonic mode

The equivalence with the forced mass-spring oscillator would not be complete without recognizing the out of sight resonant features of the amplitude variations with respect to the cavity decay rate. A few carefully chosen population oscillations clearly indicate increasing and decreasing amplitudes when κ scans from low to high values, as shown in figure 4.

Close inspections of the oscillations represented in figure 4 indicate that d_0 follows the variations of the steady-state population-inversion values. For small enough electric-field perturbation e

$$d_0(\kappa) \cong -D_0(\kappa) = \frac{1}{2C} = \frac{\kappa - 2}{\kappa(\kappa + 4)} \tag{11}$$

Just like the resonant curve of a forced mass-spring oscillator [figure E2, appendix D], d_0 follows figure 5 to exhibit a region of stronger amplitudes, cresting at $\kappa_0 = 2 + 2\sqrt{3}$. For this optimal cavity rate value, we extract from equation (11), $D_M \cong 0.067$.

The specific κ_0 value may consider as the equivalent of the mass-spring oscillator characteristic frequency $f_0 = \frac{1}{2\pi}\sqrt{\frac{k}{m}}$ at which extreme resonance occurs, amplitude response reaching its apex.

It is interesting to note that defining, as in electric circuits, a frequency bandwidth as the extent of values for which the amplitude situates in the range $D_{0M}/2 \leqslant D_0 \leqslant D_{0M}$, the corresponding κ range extends from $\kappa_m = 2.56$ to $\kappa_M = 23.29$, yielding a resonance bandwidth $\Delta\kappa = \kappa_M - \kappa_m = 20.73$.

Numerous simulated examples all converge to the conclusion that these resonant phenomena verify quite well with the original set of equation (1). All simulations follow the same amplitude scaling as the curve of figure 5. Indeed, in order to simulate small amplitude oscillations, the initial conditions, which must be the same for all κ's, call for careful choice, in order to avoid the system to diverge towards its chaotic solution. We found that the highest electric-field

Table 1. Details and coefficients relating to the analytical structures of figure 3.

κ	2.001	2.1	3.75	1000
φ	$\pi/100$	$\pi/12$	$\pi/4$	$\pi/2$
E_0	109.6	11.3	3.95	33
e	3.4	1.25	0.55	15
D_0	0	−0.01	−0.06	−0.001
d_0	0.016	0.055	0.07	0.022

initial perturbation to keep the system from diverging, inside the whole domain of the unique control parameter κ, is $e = -0.7$. The initial condition for the electric field fixing to $E = E_0 + e$ for each κ value.

Let us note that, to allow for first-glance comparison, attached to all four solutions appearing in figure 4 the same vertical scale. The harmonic part of the population scales in exact proportions to that of the steady state value. While for $\kappa = 2.1$, the oscillation takes place with small amplitude, it gradually grows to attain its peak at $\kappa = 2 + 2\sqrt{3}$, before lessening again, in a qualitatively and quantitatively perfect agreement with the steady-state-population resonant-curve of figure 5. Even though the oscillation amplitudes, as obtained from the original set equation (1), scale according to $d_0 = D_0$, a comparable amplitude value evaluates directly from the in-phase and out-of-phase amplitudes d_1 and d_2, through $d_0 = \sqrt{d_1^2 + d_1^2}$ (see appendix A for details) with, again, a sole dependence on κ ($\gamma = 1$).

Let us note that the general aspect of the graphs $D_0(\kappa)$ and $d_0(\kappa)$ is the same. The slight quantitative differences appear as follow. While the $D_0(\kappa)$ characteristic decay rate is $\kappa_0 = 2 + 2\sqrt{3} \cong 5.46$, that of $d_0(\kappa)$ is $\kappa_0' \cong 4.21$. The $d_0(\kappa)$ amplitude is half its maximum value for $\kappa_m = 2.2$ and $\kappa_M = 17.9$, implying a $\Delta\kappa \cong 15.7$ bandwidth (compare to the $\Delta\kappa \cong 20.7$ associated to the $D_0(\kappa)$ curve). Surprising is the fact that the $d_0(\kappa)$ graph delimits, satisfactorily, the region of chaotic solutions, obviously suggesting that chaos may consider the result of a resonant phenomenon typical of the Lorenz-Haken equations (added clarifications put forward in appendix C).

As extensive numerical analyses indicate, soft solutions characterize the non-linearly coupled equations for small perturbations only. The system rapidly diverges towards strong-harmonic oscillations for slightly different initial conditions. Therefore, the next step consists in the analysis of the second-order differential equation to extract further evidence pertaining to the nonlinear oscillator propensity to describe both the soft and strong amplitude dynamics.

4. The strong harmonic mode

For quick comparisons, we shall follow the same presentation scheme as that of the small amplitude case of section 3.

4.1. Phase mismatch factor

As already mentioned, the small amplitude orbits of section 3 become rapidly unstable to end-up in trajectories for which the electric field and population inversion undergo strong oscillations, around zero mean-value for $E(t)$ and $D_0 = -\frac{1}{2C}$ for $D(t)$. Outside the chaotic region, for low and high cavity decay rates, the general solution for $E(t)$ is a Fourier expansion, with an exclusive odd spectral parity, developing as [7, 13]

$$E(t) = \sum_{n=1}^{N} E_{2n+1} \cos[(2n+1)\omega t]. \tag{12}$$

Full plugging equation (12) into equation (3) yields numerous (theoretically infinite) and inextricable expressions, out of which no information is easy to pull out. A reasonable procedure consists in considering the effect of each harmonic separately.

Let us start with the fundamental component

$$e_1(t) = E_1 \cos(\omega t), \tag{13a}$$

for the field, and

$$\dot{e}_1(t) = -\omega E_1 \sin(\omega t), \tag{13b}$$

for its derivative.

Calling for elementary trigonometry, the forcing terms in equation (3) gather as

$$e_1^2(t) = E_1^2(t)\cos^2(\omega t) = E_1^2 \frac{1 + \cos(2\omega t)}{2}, \tag{13c}$$

$$\begin{aligned} e_1(t)\dot{e}_1(t) &= -\omega E_1^2 \sin(\omega t)\cos(\omega t) \\ &= -\frac{1}{2}\omega E_1^2 \sin(2\omega t), \end{aligned} \tag{13d}$$

$$\dot{e}_1^2(t) = \omega^2 E_1^2 \sin^2(\omega t) = \omega^2 E_1^2 \frac{1 - \cos(2\omega t)}{2}, \tag{13e}$$

transforming equation (3) into (see appendix A for main algebra)

$$\begin{aligned} &\frac{1}{\gamma}\ddot{D}(t) + \dot{D}(t) + E_1^2 \frac{1 + \cos(2\omega t)}{2} D(t) \\ &= \frac{1}{2C}\frac{1}{2}\left(\frac{\omega^2 E_1^2}{\kappa} - E_1^2\right) - \frac{1}{2C}\frac{1}{2}\left(\frac{\omega^2 E_1^2}{\kappa} + E_1^2\right) \\ &\times \cos(2\omega t) - \frac{1}{2C}\frac{\omega E_1^2}{2}\left(1 - \frac{1}{\kappa}\right)\sin(2\omega t) \end{aligned} \tag{14}$$

The driving constituents assemble as

$$f(t) = a_0 + a_1 \cos(2\omega t) + a_2 \sin(2\omega t), \tag{15a}$$

imposing a similar expression to the population response

$$D_2(t) = D_{02} + d_{1-2}\cos(2\omega t) + d_{2-2}\sin(2\omega t). \tag{15b}$$

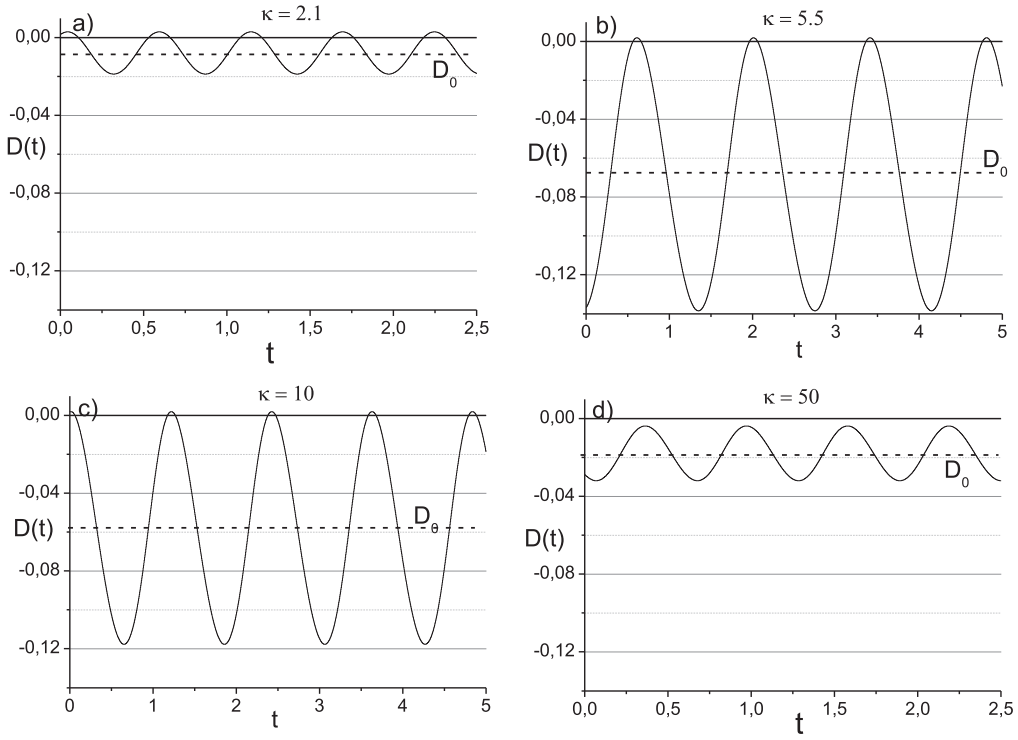

Figure 4. Population amplitudes, consequent to κ increase; (a) $\kappa = 2.1$, (b) $\kappa = 5.5$, (c) $\kappa = 10$, and (d) $\kappa = 50$.

Likewise, one may easily verify that any high-order harmonic

$$e_{2n+1}(t) = E_{2n+1}\cos((2n+1)\omega t), \tag{16a}$$

expands the driving excitation into

$$f(t) = f_c + f_1\cos(2(2n+1)\omega t) + f_2\sin(2(2n+1)\omega t), \tag{16b}$$

forcing the population response to develop according to

$$D_{2n}(t) = D_{02n} + d_{1-2n}\cos(2n\omega t) + d_{2-2n}\sin(2n\omega t) \tag{16c}$$

From these elements, it becomes obvious that, driven with an electric field expansion analogous to equation (12), the population inversion is bound to develop with an exclusive even parity

$$D(t) = D_c + \sum_{n=1}^{N} D_n\cos(2n\omega t - \varphi'). \tag{17}$$

Such an expression holds here a fundamental validity, giving credit to the Lorenz-Haken dynamics analytical-framework, which we intuitively proposed to retrieve a few phase space portraits replicating their numerical counterparts [13].

To find-out how these results allow for regular orbit description with closed-form expressions, let us first look for a phase relationship, limiting equation (17) to its second-order harmonic. Assuming

$$D(t) = D_c + d_0\cos(2\omega t - \varphi') = d_{1-2}\cos(2n\omega) + d_{2-2}\sin(2n\omega t) \tag{18}$$

From equation (14), we extract

$$\tan(\varphi') = \frac{d_{2-2}}{d_{1-2}} = \frac{(\kappa-1)\left(-\frac{4\omega^2}{\gamma}+\frac{E_1^2}{2}\right)+2\omega^2}{\left(-\frac{4\omega^2}{\gamma}+\frac{E_1^2}{2}-2(\kappa-1)\right)\omega} \tag{19a}$$

Transforming, with $E_1^2 = 2E_0^2$ and $\omega^2 = \omega_0^2$ (see appendix A for main algebra), into

$$\tan(\varphi') = \frac{7\kappa^2-13\kappa+2}{9\kappa^2-\kappa+2}\sqrt{\frac{(\kappa+1)(\kappa-2)}{2\kappa}} \tag{19b}$$

Revealing, as in the case of soft harmonics, an exclusive dependence on the cavity decay-rate κ (for simplifying purposes, and without loss of generality, we inferred $\gamma = 1$ [12]).

Similarly, two specific values appear, $\varphi'(\kappa) = 0$, for $\kappa = 2$, and $\varphi'(\kappa) \to \frac{\pi}{2}$, when $\kappa \to \infty$. However, inside the whole κ range, $\varphi'(\kappa)$ undergoes some appreciable lowering with respect to the small-amplitude $\varphi(\kappa)$, as evidenced in the representations of figure 7. For comparison, the small and strong amplitude phase-mismatch outline in the same figure.

4.2. Amplitude characteristics

In the strong harmonic regime, the original equation (1) deliver solutions with much higher amplitudes for all three variables. The electric field and polarization both oscillate around zero mean values, while the (normalized) population amplitude does not undergo sensible variations for periodic solutions. Figure 8 indicates that d_0 evolves with maximum values not exceeding 0.4. Let us insist again on the fact that

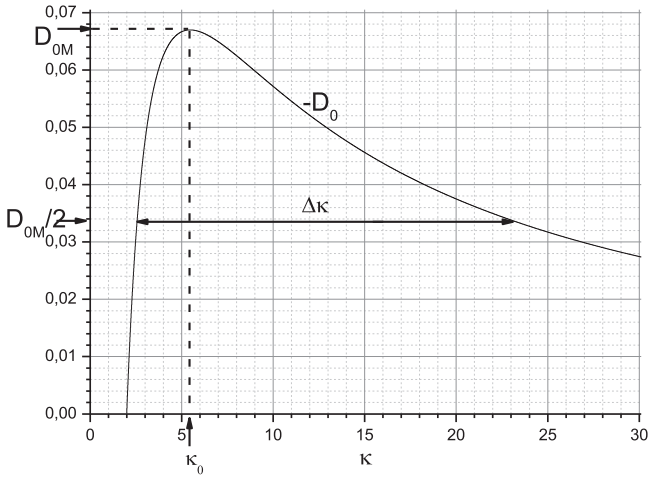

Figure 5. Population steady state as a function of the cavity decay rate κ. Consistent with the external excitation 2 C, it also characterizes some resonant response of the population oscillator submitting to an electric-field perturbation $e\cos(\omega t)$.

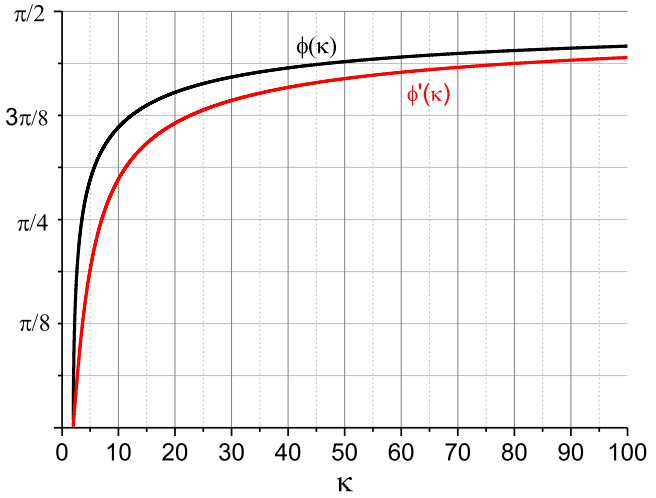

Figure 7. Graphical representation of the phase difference with respect to the cavity decay-rate κ, corresponding to the small (upper trace) and strong (lower trace) harmonic cases, indicative of phase lowering for the strong-amplitude mode.

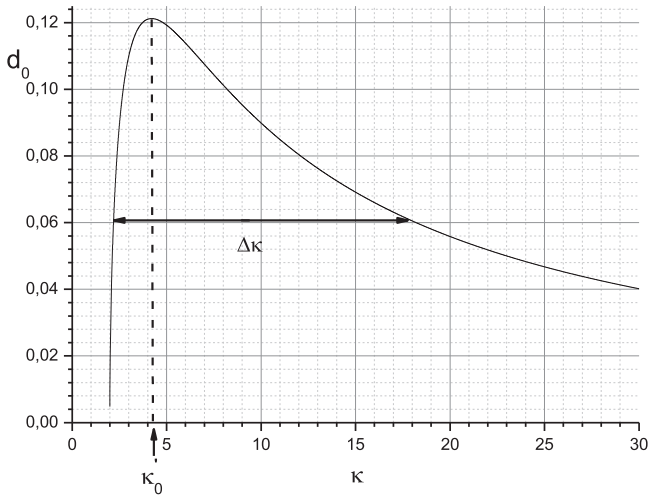

Figure 6. Resonant response to a perturbing electric field $e\cos(\omega t)$, describing the amplitude development d_0 with respect to the cavity decay rate κ.

the κ values, deliberately selected outside the chaotic region, cover a large span inside which the solution is a period-one signal.

If adapted, the oscillator model should recover, at least qualitatively, these results. Likewise, evaluating the in-phase and out-phase population components d_{1-2} and d_{2-2}, accordingly yields $d_0 = \sqrt{d_{1-2}^2 + d_{2-2}^2}$ (see appendix A for detailed algebra), strictly relating to the cavity decay rate

As compared to steady state, the $d_0(\kappa)$ graph, represented in figure 9, shows higher amplitudes for low κ values. However, a single glance to figure 8 reveals that the numerical population amplitude does not compare to what equation (20) figures out.

Such easy to understand discrepancies call for useful comments and adjustments. Contrary to the small amplitude regime, for which the signal follows a simple first-order cosine for all three variables, the strong harmonic solutions expand according to equation (12) for the electric field and equation (17) for the population inversion. However, the analysis limited the developments to first orders only. In so doing, a great part of the field and population disregard. These must take into account for better agreements with the numerical solutions.

To find out how to do so, let us explore a few periodic solutions through spectra representations, with various κ values. Figure 10 is a series of Fast-Fourier-Transforms generated with typical time traces of the electric-field signals.

The spectra indicate that for the lower range of κ value ($2 \leqslant \kappa \leqslant 2.11$) for which the solution is and S1 orbit, the electric field expansion limits to dominant first and third order components. Analytically, these structures describe with

$$E(t) \cong E_M \cos^3(\omega t), \tag{21a}$$

However, with higher κ's (and in the range of period-one solutions), the signals expand with increasing cosine

$$d_0 = \frac{2(\kappa+1)(\kappa+2)}{\kappa(\kappa+4)} \frac{\sqrt{[2(\kappa-1)(\kappa-2)+(\kappa+1)(7\kappa-2)]^2 + \frac{(\kappa+1)(\kappa-2)}{2}[(\kappa-1)(7\kappa-2)-4\kappa]^2}}{(\kappa+1)(7\kappa-2)^2 + 8\kappa(\kappa-2)} \tag{20}$$

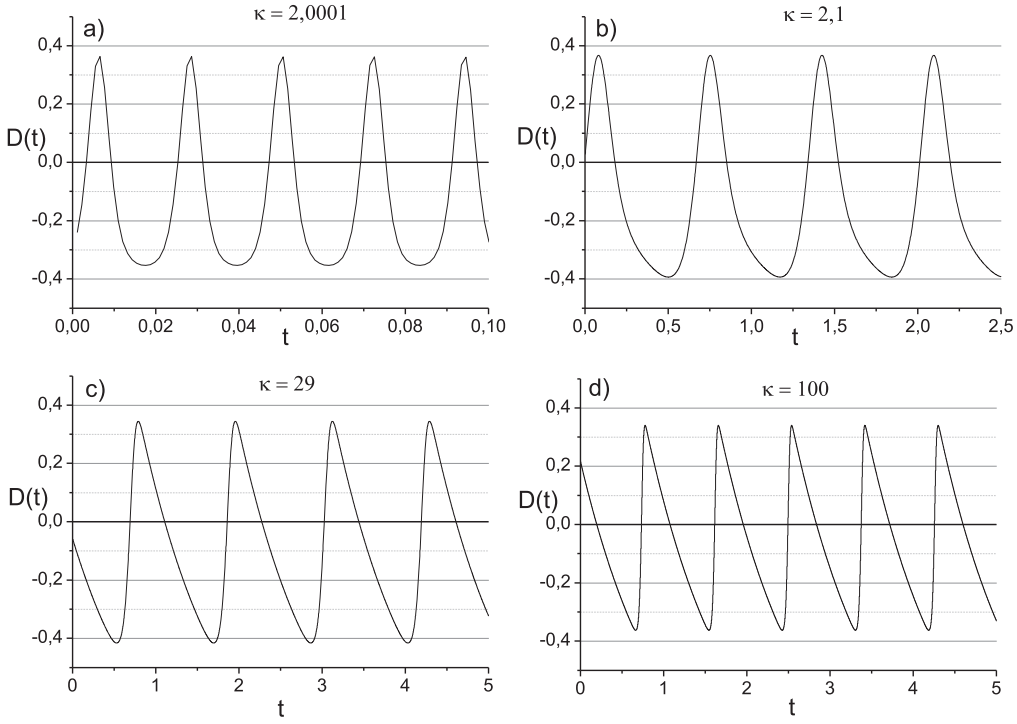

Figure 8. Population inversion signals obtained numerically with (a) $\kappa = 2.0001$, (b) $\kappa = 2.1$, (c) $\kappa = 29$, and (d) $\kappa = 100$, showing identical oscillation-amplitudes.

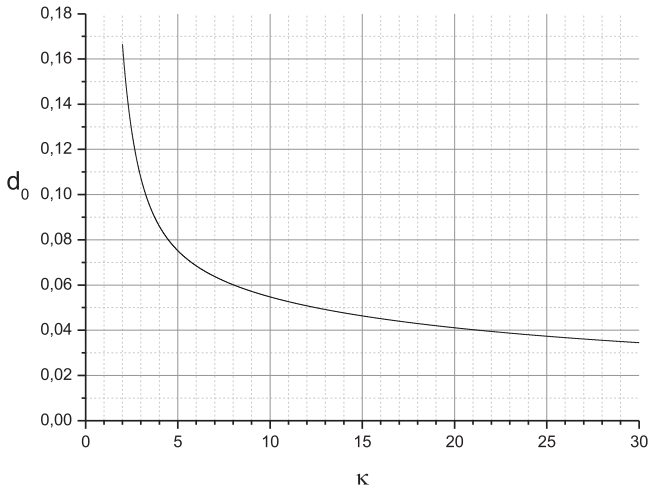

Figure 9. Graphical representation of the population amplitude with respect to the cavity decay-rate κ, considering the first-order electric-field amplitude only.

exponent

$$E(t) \cong E_M \cos^{11}(\omega t), \tag{21b}$$

for $\kappa = 29$, and

$$E(t) \cong E_M \cos^{21}(\omega t) \tag{21c}$$

for $\kappa = 100$.

A common signature to these solutions is the general expression

$$E(t) \cong E_M \cos^{m}(\omega t) \tag{22}$$

Empirically, integer m approximates in terms of the cavity decay rate as $m \cong 2\sqrt{\kappa}$.

As a consequence, adapted modifications should take into account these peak-intensity variations, which constrain the electric field and population amplitudes to evolve according to $E_M \cong 2\sqrt{\kappa}E_0$, and $d_M \cong 2\sqrt{\kappa}d_0$.

With these simple revisions, we retrieve for the population amplitudes, more accurate values, as indicated in the graph of figure 11. Consistent with the numerical time traces of figure 8, the population amplitude clamps to values close to 0.4, for any cavity decay-rate κ, comprising the chaotic window.

4.3. Analytical solutions

To confirm further the nonlinear oscillator assets, let us represent a few numerically simulated solutions, in the population versus electric-field phase-space.

The examples in figure 12 correspond to control-parameter values that deliver periodic S1 solutions. Starting with $\kappa = 2.0001$, the trajectory consists of a parabola. The system perpetually oscillates from one tip to the other, with no phase difference between the electric field and population inversion. Analytically, the orbit of figure 12(a) describes with

$$E(t) = E_M \cos(\omega t), \tag{23a}$$

$$D(t) = D_c + d_M \cos(2\omega t). \tag{23b}$$

However, the value $\frac{1}{2C} \cong 8.10^{-6} \ll d_M \cong 0.4$, disregards the D_c term in equation (23*b*), thus imposing the population to evolve according to

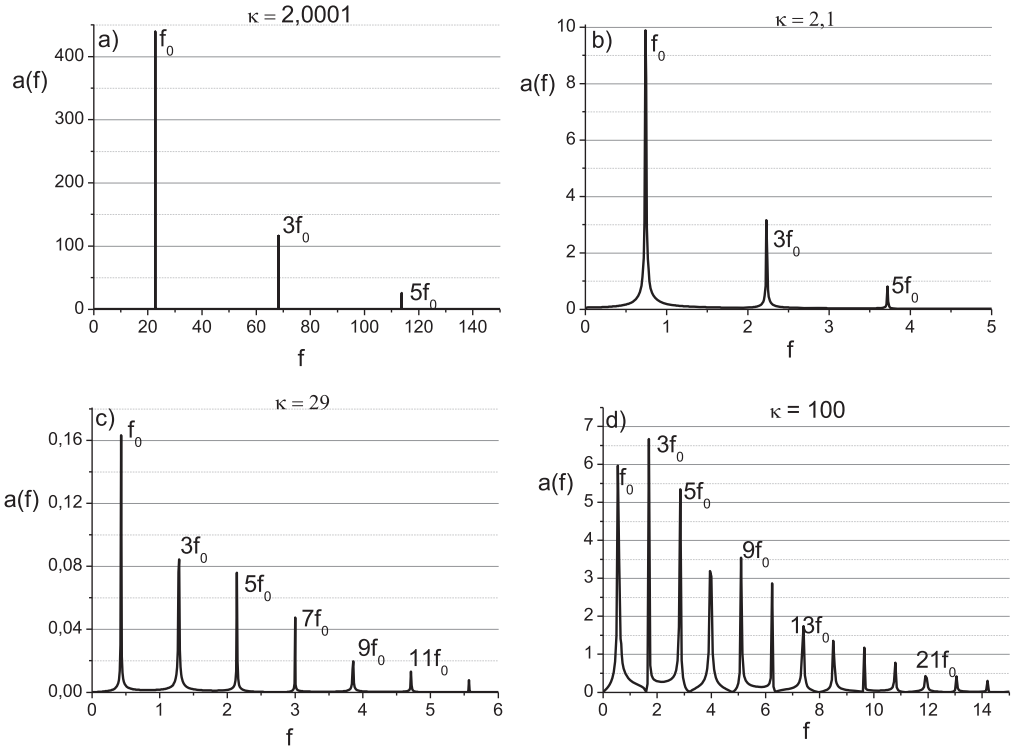

Figure 10. Electric-field spectra, simulated from equation (1) and corresponding time traces (a) $\kappa = 2.0001$, (b) $\kappa = 2.1$, (c) $\kappa = 29$, and (d) $\kappa = 100$. Note the third-order amplitude growth with increasing κ.

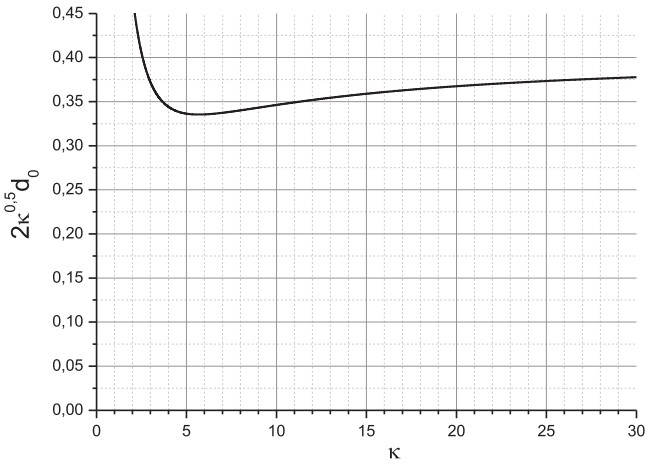

Figure 11. Adjusted population amplitude with respect to κ, considering the effective peak amplitude of the electric-field and its direct impact on $D(t)$.

$$D(t) = d_M \cos(2\omega t) \tag{23c}$$

Complying with an in-phase fit to the electric field.

For $\kappa = 2.01$, the parabola converts into some symmetric loop with thin branches. The phase difference between the electric field and population becoming more significant, increasing according to equation (19b), and the lower graph of figure 7. For $\kappa = 2.1$, the closed orbit expands further, turning out thicker to follow figure 12(c), before fully stretching out, for $\kappa = 29$. All four orbits symmetry is of the S1 type [12], describing with

$$E(t) = E_M \cos(\omega t), \tag{24a}$$

$$D(t) = D_c + d_M \cos(2\omega t + \varphi'). \tag{24b}$$

Analytical counterparts of the numerically simulated trajectories gather in figure 13. The corresponding coefficients collect in table 2 for quick representations with any graphical software, including that of a pocket calculator.

Let us note that, for $\kappa = 2_+$, the phase difference is almost half that of the small harmonic case. This is of no surprise, either. Since, when the small oscillations around steady state convert into strong amplitude signals, a slowing down effect occurs, the frequency and phase both shifting towards lower values. This behavior verifies numerically with the simulated signals for $\kappa = 2_+$. For example, for $\kappa = 2.1$, the time lag between the field and population inversion scales as $\Delta t = 0.02$, and a corresponding period $T_{st} = 0.55$, implying $\varphi \cong 2\pi\dfrac{\Delta t}{T_{st}} \cong \dfrac{\pi}{12}$, for the small amplitude oscillations; while measuring $\Delta t = 0.01$, and a period between pulses $T_p = 0.7$ (population inversion period), indicates $\varphi' \cong 2\pi\dfrac{\Delta t}{T_p} \cong \dfrac{\pi}{35}$, for the strong harmonic case.

For high κ values, the solution converges towards the orbit of figure 12(d), obtained with $\kappa = 29$. The analytical description does not follow equations (24*a*) and (24*b*). Because, as already mentioned, for high κ's, high-order harmonics cannot be neglected. Considering the third harmonic in the electric field expansion, figure 12(d) trajectory adjusts with

$$E(t) = E_M \cos^3(\omega t), \tag{25a}$$

$$D(t) = D_c + d_M(2\omega t + \pi/2.5) \tag{25b}$$

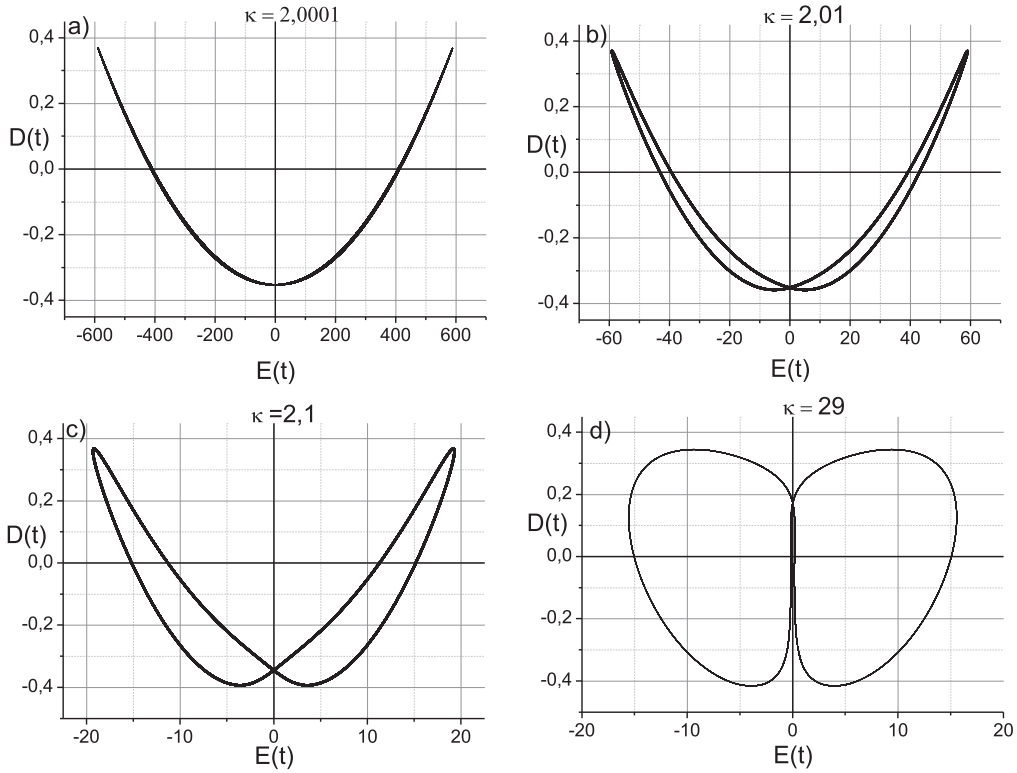

Figure 12. Numerical phase-space orbits obtained with equation (1) for (a) $\kappa = 2.0001$, (b) $\kappa = 2.01$, (c) $\kappa = 2.1$, and (d) $\kappa = 29$.

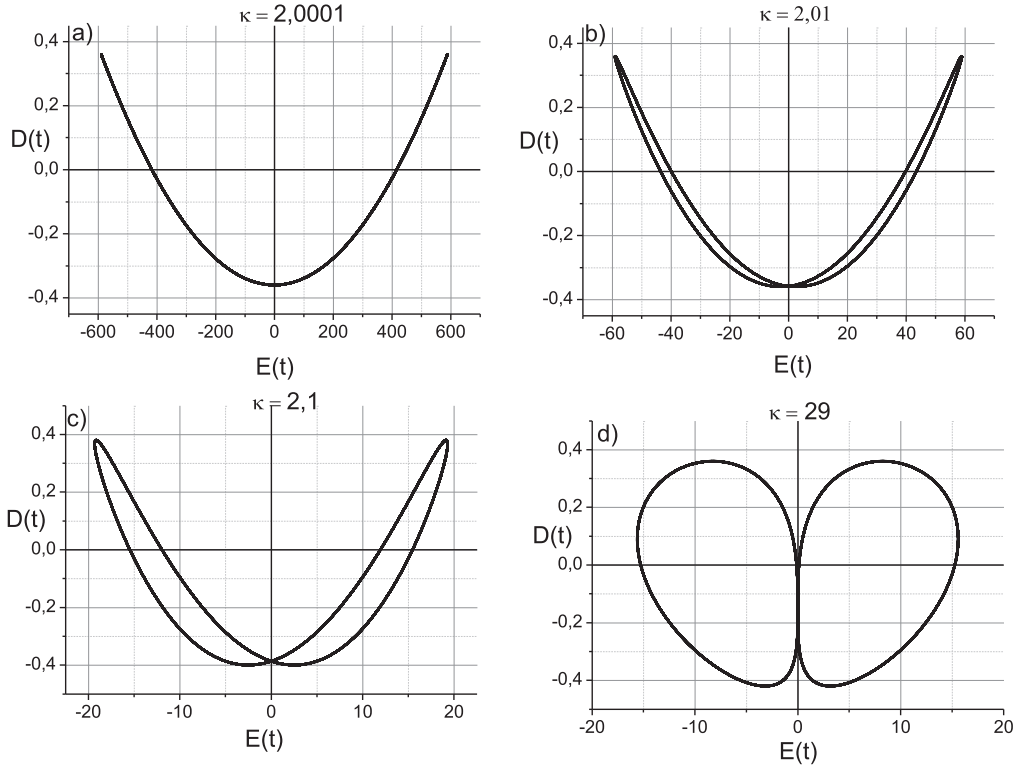

Figure 13. Analytical phase-space trajectories obtained with the coefficients of table 2. Note the equivalence with the simulated counterparts of figure 12, and the distinct orbit shaping for low and high κ's.

Table 2. Parameter and coefficient details to -figure 13- orbit modeling.

κ	2.0001	2.01	2.1	29
φ'	0	$\pi/64$	$\pi/24$	$\pi/2.5$
E_M	589	59	19.3	15.6
D_c	0	0	−0.01	−0.03
d_M	0.36	0.36	0.39	0.39

Indeed, equation (25*a*) contains both the fundamental and the third harmonic components. Since

$$\cos^3(x) = \frac{3}{4}\cos(x) + \frac{1}{4}\cos(3x), \tag{26a}$$

Equation (25*a*) is equivalent to

$$E(t) = E_1\cos(\omega t) + E_3\cos(3\omega t), \tag{26b}$$

with $E_1 = \frac{3}{4}E_M$, and $E_3 = \frac{1}{4}E_M$.

These adjustments best understand with the electric field Fourier-spectra represented in figure 10. For low κ's, the fundamental frequency dominates, as in the example of figures 10(a) and (b), obtained respectively with $\kappa = 2.0001$ and $\kappa = 2.1$. This justifies the limited to first order development in equation (24*a*). However, for high cavity decay rates, spectra become broader, exhibiting numerous high order components with protruding amplitudes. The third one scales approximately half the amplitude of the fundamental frequency f_0, for the $\kappa = 29$-example of figure 10(c), justifying the third order electric-field development in equation (25*a*) used to describe the corresponding phase space portrait of figure 13(d), while time signal representations require higher order developments, as equation (21*c*). Increasing κ further, the spectra enlarge to contain up to the twenty-first harmonic, while the third order dominates the first one, an example of which represents in figure 10(d), with $\kappa = 100$.

These examples, selected among a wealth of others, deliberately focused on the control parameter space inside which periodic and symmetric trajectories are the rule. A main conclusion to draw is the fact that contrary to the soft case, for which the method applies to any control-parameter value, the strong amplitude analysis cannot apply to describe any irregular orbit. Yet, the resonance curve may serve as a reference chart to delimit the range of cavity decay rates inside which chaos takes place (see further clarifications in appendix C). Nonetheless, the perfect match between the computer solutions and their analytical descriptions suffers no ambiguity with respect to the second-order nonlinear oscillator approach. It has probably much to offer in terms of modelling asymmetric and higher order periodicities. Further inspections are in progress.

5. Auxiliary clarifications

The second order population oscillator constructing with the combination of two equations out of three, one may wonder whether the third one, i.e. Equation (1*b*), is of no use, therefore dismissible. In fact, it is not! It is not a difficult task either to demonstrate that the above results do not contradict the polarization dynamic, as conforming to equation (1*b*). To do so, let us combine equations (2*a*) and (2*b*) and derive an equation for the electric field, reorganizing in the form

$$\ddot{E}(t) + (\kappa+1)\dot{E}(t) + \kappa E(t) + 2C\kappa E(t)D(t) = 0 \tag{27}$$

This equation is of the second-order differential type for the electric field, with the population as the driving variable. Let us limit the analysis to the small harmonic case and find out which information may extract from it.

In response to a driving population

$$D(t) = D_0 + d\cos(\omega t) \tag{28a}$$

The electric field and derivatives follow

$$E(t) = E_0 + e_1\cos(\omega t) + e_2\sin(\omega t) \tag{28b}$$

$$\dot{E}(t) = -e_1\omega\sin(\omega t) + e_2\omega\cos(\omega t) \tag{28c}$$

$$\ddot{E}(t) = -e_1\omega^2\cos(\omega t) - e_2\omega^2\sin(\omega t) \tag{28d}$$

Limiting all developments to first order terms, we arrive at

$$[e_2(\kappa+1)\omega - e_2\omega^2 + 2C\kappa E_0 d]\cos(\omega t) + [-e_1(\kappa+1)\omega - e_2\omega^2]\sin(\omega t) = 0 \tag{29a}$$

From which we obtain

$$\frac{e_2}{e_1} = -\frac{\kappa+1}{\omega} = -\sqrt{\frac{(\kappa+1)(\kappa-2)}{2\kappa}} \tag{30a}$$

The rearrangement

$$E(t) = E_0 + e_1\cos(\omega t) - \frac{\kappa+1}{\omega}e_1\sin(\omega t) = E_0 + e\cos(\omega t + \varphi_{e-d}) \tag{30b}$$

yields

$$\tan(\varphi_{e-d}) = -\sqrt{\frac{(\kappa+1)(\kappa-2)}{2\kappa}} \tag{31a}$$

and

$$e = \frac{\kappa^2(\kappa+4)}{(\kappa-1)}\sqrt{\frac{\kappa^2+\kappa-2}{2\kappa(\kappa+2)(\kappa+1)(\kappa-2)}}\,d \tag{31b}$$

i.e. the exact replicas of equation (9*b*), for the phase, and (A5b), for the amplitude!

The two equations (3*a*) and (27) represent two coupled second order differential equations whose dynamics conforms to the Lorenz equations. The effect of the polarization takes into account through equation (2*a*). Indeed, at first glance, the oscillator expressions seem more complicated than the original 3D set. However, they offer interesting shortcuts towards the physics that hides behind some of the complex dynamics. The one population oscillator is all it takes to clear up the trajectory subtleties.

6. Conclusion and prospective

This paper main objective -that of constructing a second-order oscillator from the Lorenz equations- fully fulfills. Extracting

new and genuine information has led to represent coherent-light-matter- interactions during unstable operation, in the easiest way possible. With this respect, investigations and outcomes are quite satisfactory.

Let us recall that from the early days of nonlinear dynamics, phase-space representations put in use as crucial tools to describe and ascertain unsteady solutions and characteristics. However, no author thought of considering phase identifications and quantifying, the missing clues for closed-form expressions and analytical trajectory-descriptions. While, the second-order oscillator clarifies it all.

Also worth emphasizing on is that if Laser physicists put their main attention on the field-intensity output, it is because it represents the system's sole observable, monitoring on an oscilloscope screen with adapted sensors. Yet, as a macroscopic source, summed over microscopic dipoles, the untraceable population dynamics plays a significant role. Our study making it plain and visible.

Indeed, transforming the three nonlinearly coupled differential equations, which govern the dynamics of a single mode homogeneously broadened laser, into a second-order differential equation, reminiscent of a forced harmonic oscillator, should switch-off the 3D trajectories, if numerically solved without imposing any initial harmonic structure to the electric field. Similarly, the mass-spring system comes at rest, with no external excitation. Nonetheless, from purportedly harmonic fields, conforming to the numerical solutions, we extracted new analytical information and properties showing that, in the control parameter space of periodic solutions, some suitably quantifiable phase difference between the electric field and population inversion plays an essential role in orbit shaping. Additional projections seem to indicate that apart from chaotic trajectories, the approach may apply, as well, to symmetric and asymmetric cascading with higher periodicities. Further modelling is necessary.

Appendixes

Foreword: a good part of the algebra presented in the following is time-consuming, but not -even though it may seem- awkward. Thanks to the 'copy and paste' action in the Word-Equation functionality, calculus becomes quite easy and comforting to carryout. Its use highly recommends.

Appendix A

A.1. Population amplitude and phase-relationship in the small-harmonic regime

The electric field and population signals, with their derivatives, develop according to

$$E(t) = E_0 + e\cos(\omega t), \tag{A1a}$$

$$\dot{E}(t) = -e\omega\sin(\omega t), \tag{A1b}$$

$$D(t) = D_0 + d_1\cos(\omega t) + d_2\sin(\omega t), \tag{A1c}$$

$$\dot{D}(t) = -d_1\omega\sin(\omega t) + d_2\omega\cos(\omega t), \tag{A1d}$$

$$\ddot{D}(t) = -d_1\omega^2\cos(\omega t) - d_2\omega^2\sin(\omega t). \tag{A1e}$$

Injecting each term into the equation

$$\frac{1}{\gamma}\ddot{D}(t) + \dot{D}(t) + E(t)^2D(t) = \frac{1}{2C}\left(E(t)\dot{E}(t)\left(1 - \frac{1}{\kappa}\right) + \frac{\dot{E}(t)^2}{\kappa} - E(t)^2\right) \tag{A2}$$

limiting the developments to first-order amplitudes, we obtain

$$\begin{aligned}&\left(-d_1\frac{\omega^2}{\gamma} + d_2\omega + 2eE_0D_0 + E_0^2d_1\right)\cos(\omega t)\\ &+\left(-d_2\frac{\omega^2}{\gamma} - d_1\omega + E_0^2d_2\right)\sin(\omega t) + E_0^2D_0\\ &\cong -\frac{1}{2C}e\omega E_0\sin(\omega t)\left(1 - \frac{1}{\kappa}\right) - \frac{1}{2C}E_0^2\\ &-\frac{1}{2C}2eE_0\cos(\omega t)\end{aligned} \tag{A3a}$$

Equating similar terms in the right and left-hand sides; noting that $E_0^2D_0 = -\frac{1}{2C}E_0^2$ and $2eE_0D_0 = -\frac{1}{2C}2eE_0$, we end-up with

$$\left(\frac{\omega^2}{\gamma} - E_0^2\right)d_1 - \omega d_2 = 0, \tag{A3b}$$

$$\left(\frac{\omega^2}{\gamma} - E_0^2\right)d_2 + \omega d_1 = \frac{1}{2C}e\omega E_0\left(1 - \frac{1}{\kappa}\right), \tag{A3c}$$

from which, we readily extract equations (6*d*) and (6*e*) of the text, converting into

$$d_1 = e\frac{\sqrt{(\kappa-2)(\kappa+1)(\kappa+2)}}{\kappa(\kappa+4)}\frac{2(\kappa-1)}{2\kappa+(\kappa+1)(\kappa-2)} \tag{A4a}$$

$$d_2 = e\frac{\sqrt{2\kappa(\kappa+2)}}{\kappa^2(\kappa+4)}\frac{(\kappa-2)(\kappa+1)(\kappa-1)}{2\kappa+(\kappa+1)(\kappa-2)} \tag{A4b}$$

In order to complete the quantitative elements associated to the small amplitude dynamics, we must derive an expression for the real population amplitude. It forthrightly stems from equations (6*d*) and (6*e*) as

$$d_0 = \sqrt{d_1^2 + d_1^2} = \frac{1}{2C}eE_0\left(1 - \frac{1}{\kappa}\right) \times \frac{1}{\sqrt{1 + \omega^2\left(\frac{1}{\gamma} - \frac{E_0^2}{\omega^2}\right)^2}} \tag{A5a}$$

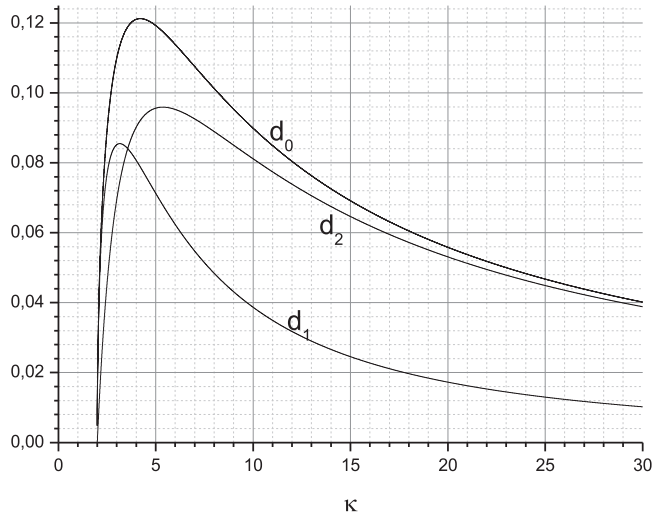

Figure A1. In-phase d_1, out-of-phase d_2, and real amplitude d_0, of the population components, with respect to the cavity decay rate, obtained in the small amplitude regime.

Which, with equations (7*a*) and (7*b*), takes the form (assuming $\gamma = 1$)

$$d_0 = e\frac{\kappa - 1}{\kappa^2(\kappa + 4)}\sqrt{\frac{2\kappa(\kappa - 2)(\kappa + 1)(\kappa + 2)}{2\kappa + (\kappa + 1)(\kappa - 2)}} \tag{A5b}$$

The population amplitude follows a resonant curve with clear similarities with that of a mass-spring oscillator, the cavity decay rate playing the same role as the excitation frequency of the external driving force applied to the mechanical system.

The general aspect of the population-amplitude $d_0(\kappa)$ approximately follows that of the steady state figure 5, with quite noticeable resonant features, appearing in Figure A1. Included for comparison are the in-phase $d_1(\kappa)$ and out-phase $d_2(\kappa)$ components, indicating a region of strong competition before $d_1(\kappa)$ goes to zero for high κ values, signifying a tendency towards some phase-quadrature evolution between the electric field and population inversion.

Appendix B

B.1. Population amplitude and phase-relationship in the strong-harmonic regime

The dominant part of an electric field expansion of the form equation (12) is the first order component

$$e_1(t) = E_1\cos(\omega t). \tag{B1a}$$

The following relations

$$e_1^2(t) = E_1^2(t)\cos^2(\omega t) = E_1^2\frac{1 + \cos(2\omega t)}{2}, \tag{B1b}$$

$$\begin{aligned} e_1(t)\dot{e}_1(t) &= -\omega E_1^2\sin(\omega t)\cos(\omega t) \\ &= -\frac{1}{2}\omega E_1^2\sin(2\omega t), \end{aligned} \tag{B1c}$$

$$\dot{e}(t)_1^2 = \omega^2 E_1^2\sin^2(\omega t) = \omega^2 E_1^2\frac{1 - \cos(2\omega t)}{2}, \tag{B1d}$$

transform equation (3) into

$$\begin{aligned} &\frac{1}{\gamma}\ddot{D}(t) + \dot{D}(t) + E_1^2\frac{1 + \cos(2\omega t)}{2}D(t) \\ &= -\frac{1}{2C}\frac{\omega E_1^2}{2}\left(1 - \frac{1}{\kappa}\right)\sin(2\omega t) + \frac{1}{2C}\frac{1}{2}\left(\frac{\omega^2 E_1^2}{\kappa} - E_1^2\right) \\ &\quad -\frac{1}{2C}\frac{1}{2}\left(\frac{\omega^2 E_1^2}{\kappa} + E_1^2\right)\cos(2\omega t). \end{aligned} \tag{B2}$$

The driving $\sin(2\omega t)$ and $\cos(2\omega t)$ in the right-hand side imply similar expansions for the population inversion

$$D(t) = D_0 + d_{1-2}\cos(2\omega t) + d_{2-2}\sin(2\omega t), \tag{B3a}$$

$$\dot{D}(t) = -d_{1-2}2\omega\sin(2\omega t) + d_{2-2}2\omega\cos(2\omega t), \tag{B3b}$$

$$\ddot{D}(t) = -d_{1-2}4\omega^2\cos(2\omega t) - d_{2-2}4\omega^2\sin(2\omega t) \tag{B3c}$$

Injected into equation (B2), these yield

$$\begin{aligned} &-d_{1-2}\frac{4\omega^2}{\gamma}\cos(2\omega t) - d_{2-2}\frac{4\omega^2}{\gamma}\sin(2\omega t) \\ &\quad -d_{1-2}2\omega\sin(2\omega t) + d_{2-2}2\omega\cos(2\omega t) \\ &\quad + E_1^2\frac{1 + \cos(2\omega t)}{2}(D_0 + d_{1-2}\cos(2\omega t) + d_{2-2}\sin(2\omega t)) \\ &= -\frac{1}{2C}\frac{\omega E_1^2}{2}\left(1 - \frac{1}{\kappa}\right)\sin(2\omega t) + \frac{1}{2C}\frac{1}{2}\left(\frac{\omega^2 E_1^2}{\kappa} - E_1^2\right) \\ &\quad -\frac{1}{2C}\frac{1}{2}\left(\frac{\omega^2 E_1^2}{\kappa} + E_1^2\right)\cos(2\omega t). \end{aligned} \tag{B4a}$$

The product $E(t)D(t)$ developing as

$$\begin{aligned} &E_1^2\frac{1 + \cos(2\omega t)}{2}(D_0 + d_{1-2}\cos(2\omega t) \\ &\quad + d_{2-2}\sin(2\omega t)) = \frac{1}{2}E_1^2 D_0 + E_1^2\frac{d_{1-2}}{4} + \left(E_1^2\frac{D_0}{2}\right. \\ &\quad \left. + E_1^2\frac{d_{1-2}}{2}\right)\cos(2\omega t) + E_1^2\frac{d_{2-2}}{2}\sin(2\omega t) \\ &\quad + E_1^2\frac{d_{1-2}}{4}\cos(4\omega t) + E_1^2\frac{d_{2-2}}{4}\sin(4\omega t) \end{aligned} \tag{B4b}$$

Collecting terms in $\cos(2\omega t)$ and $\sin(2\omega t)$, we obtain

$$\begin{aligned} &\left(-d_{1-2}\frac{4\omega^2}{\gamma} + d_{2-2}2\omega + E_1^2\frac{D_0}{2} + E_1^2\frac{d_{1-2}}{2}\right)\cos(2\omega t) \\ &\quad -\left(d_{2-2}\frac{4\omega^2}{\gamma} + d_{1-2}2\omega - E_1^2\frac{d_{2-2}}{2}\right)\sin(2\omega t) \\ &\quad +\frac{1}{2}E_1^2 D_0 + E_1^2\frac{d_{1-2}}{4} + E_1^2\frac{d_{1-2}}{4}\cos(4\omega t) \\ &\quad +E_1^2\frac{d_{2-2}}{4}\sin(4\omega t) = -\frac{1}{2C}\frac{\omega E_1^2}{2}\left(1 - \frac{1}{\kappa}\right)\sin(2\omega t) \\ &\quad +\frac{1}{2C}\frac{1}{2}\left(\frac{\omega^2 E_1^2}{\kappa} - E_1^2\right) - \frac{1}{2C}\frac{1}{2}\left(\frac{\omega^2 E_1^2}{\kappa} + E_1^2\right)\cos(2\omega t) \end{aligned} \tag{B4c}$$

From which we infer

$$-d_{1-2}\frac{4\omega^2}{\gamma}+d_{2-2}2\omega+E_1^2\frac{d_{1-2}}{2}=-\frac{1}{2C}\frac{1}{2}\frac{\omega^2E_1^2}{\kappa}, \quad \text{(B5}a\text{)}$$

$$-d_{2-2}\frac{4\omega^2}{\gamma}-d_{1-2}2\omega+E_1^2\frac{d_{2-2}}{2}=-\frac{1}{2C}\frac{\omega E_1^2}{2}\left(1-\frac{1}{\kappa}\right)$$
$$=-\frac{1}{2C}\frac{\omega^2E_1^2}{2}\frac{\kappa-1}{\omega}, \quad \text{(B5}b\text{)}$$

combining into

$$\left(-\frac{4\omega^2}{\gamma}+\frac{E_1^2}{2}-2(\kappa-1)\right)\omega d_{2-2}$$
$$=\left\{(\kappa-1)\left(-\frac{4\omega^2}{\gamma}+\frac{E_1^2}{2}\right)+2\omega^2\right\}d_{1-2}, \quad \text{(B5}c\text{)}$$

to yield

$$\frac{d_{2-2}}{d_{1-2}}=\tan(\varphi')=\frac{(\kappa-1)\left(-\frac{4\omega^2}{\gamma}+\frac{E_1^2}{2}\right)+2\omega^2}{\left(-\frac{4\omega^2}{\gamma}+\frac{E_1^2}{2}-2(\kappa-1)\right)\omega}. \quad \text{(B5}d\text{)}$$

This last relation quantifies the phase difference between the electric field and population signal, in the strong amplitude case. Likewise, it transforms into an expression with as the sole variable, with adapted clues and procedures, hereafter summarized.

Setting $E(t)=E_1\cos(\omega t)$ points toward $<E^2(t)>=\frac{E_1^2}{2}\cong E_0^2$

Therefore, with $E_1^2=2E_0^2=2\frac{(\kappa+1)(\kappa+2)}{\kappa-2}$, and $\omega^2=\omega_0^2=\frac{2\kappa(\kappa+1)}{\kappa-2}$, we obtain

$$\frac{d_{2-2}}{d_{1-2}}=\tan(\varphi')$$
$$=\frac{(\kappa-1)\left(-\frac{8\kappa(\kappa+1)}{\kappa-2}+\frac{(\kappa+1)(\kappa+2)}{\kappa-2}\right)+\frac{4\kappa(\kappa+1)}{\kappa-2}}{\left(-\frac{8\kappa(\kappa+1)}{\kappa-2}+\frac{(\kappa+1)(\kappa+2)}{\kappa-2}-2(\kappa-1)\right)}$$
$$\times\sqrt{\frac{\kappa-2}{2\kappa(\kappa+1)}} \quad \text{(B6}a\text{)}$$

transforming into

$$\frac{d_{2-2}}{d_{1-2}}=\tan(\varphi')=\frac{7\kappa^2-13\kappa+2}{9\kappa^2-\kappa+2}\sqrt{\frac{(\kappa+1)(\kappa-2)}{2\kappa}} \quad \text{(B6}b\text{)}$$

From equations (B5*a*) and (B5*b*) also derive the following expressions for the in-phase and out-of-phase population amplitudes

$$d_{1-2}=\frac{1}{2C}\frac{E_1^2}{2}\frac{\omega^2}{\kappa}\frac{2(\kappa-1)+\left(\frac{4\omega^2}{\gamma}-\frac{E_1^2}{2}\right)}{\left(\frac{4\omega^2}{\gamma}-\frac{E_1^2}{2}\right)^2+4\omega^2} \quad \text{(B7}a\text{)}$$

$$d_{2-2}=\frac{1}{2C}\frac{E_1^2}{2}\frac{\omega}{\gamma}\frac{(\kappa-1)\left(\frac{4\omega^2}{\gamma}-\frac{E_1^2}{2}\right)-2\omega^2}{\left(\frac{4\omega^2}{\gamma}-\frac{E_1^2}{2}\right)^2+4\omega^2} \quad \text{(B7}b\text{)}$$

Both relations transform into formulas with an exclusive dependence on the cavity decay rate

$$d_{1-2}=\frac{2(\kappa+1)(\kappa+2)}{\kappa(\kappa+4)}\frac{2(\kappa-1)(\kappa-2)+(\kappa+1)(7\kappa-2)}{(\kappa+1)(7\kappa-2)^2+8\kappa(\kappa-2)} \quad \text{(B8}a\text{)}$$

$$d_{2-2}=\frac{(\kappa+1)(\kappa+2)}{\kappa(\kappa+4)}\sqrt{\frac{2(\kappa+1)(\kappa-2)}{\kappa}}$$
$$\times\frac{(\kappa-1)(7\kappa-2)-4\kappa}{(\kappa+1)(7\kappa-2)^2+8\kappa(\kappa-2)} \quad \text{(B8}b\text{)}$$

Equations (B7*a*) and (B7*b*) combine to deduce the real population amplitude

$$d_0=\sqrt{d_{1-2}^2+d_{2-2}^2}=\frac{\frac{1}{2C}\frac{E_1^2}{2}\frac{1}{\kappa}\sqrt{\left[2(\kappa-1)+\omega^2\left(\frac{4}{\gamma}-\frac{E_1^2}{2\omega^2}\right)\right]^2+\omega^2\left[(\kappa-1)\left(\frac{4}{\gamma}-\frac{E_1^2}{2\omega^2}\right)-2\right]^2}}{\omega^2\left(\frac{4}{\gamma}-\frac{E_1^2}{2\omega^2}\right)^2+4} \quad \text{(B9}a\text{)}$$

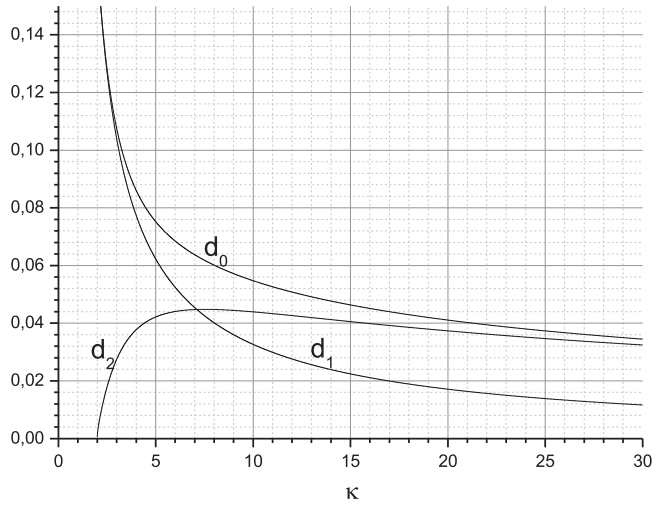

Figure B1. In-phase, out-of-phase, and real population-amplitude response to first order field-component, obtained in the strong harmonic regime.

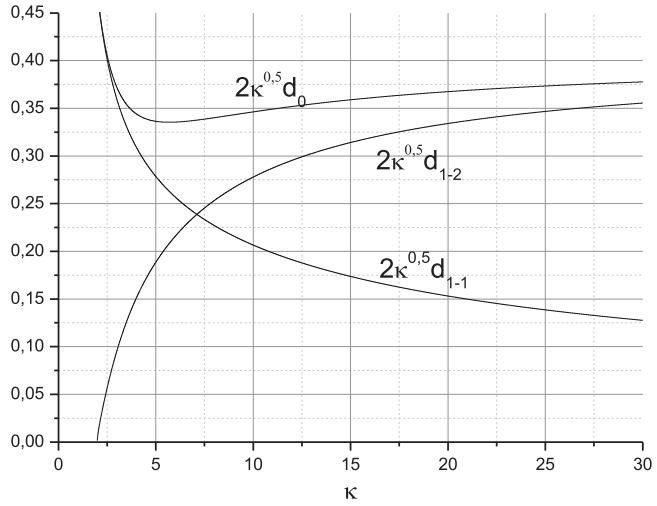

Figure B2. Actual in-phase, out of phase, and real population amplitudes, including higher order influence.

Converting into

$$d_0 = \frac{2(\kappa+1)(\kappa+2)}{(\kappa+4)} \frac{\sqrt{[2(\kappa-1)(\kappa-2)+(\kappa+1)(7\kappa-2)]^2 + \frac{(\kappa+1)(\kappa-2)}{2}[(\kappa-1)(7\kappa-2)-4\kappa]^2}}{(\kappa+1)(7\kappa-2)^2+8\kappa(\kappa-2)} \quad \text{(B9}b\text{)}$$

Equations (B8*a*), (B8*b*), and (B9*b*) follow the graphs of figure B1.

Close inspection of figure B1 reveals unfitting quantities with the numerical amplitudes that call for further adjustments. To do so, let us remind that all the strong-amplitude approach presented in the study limited to the electric-field first-order component $e_1(t) = E_1\cos(\omega t)$. However, as explained in section 4, the pulse peaks of the solutions increase with cavity decay rate, approximately scaling as $E_M \cong 2\sqrt{\kappa}E_0$ implying $d_M \cong 2\sqrt{\kappa}d_0$ for the population inversion. With this empirically admitted fact, we obtain more accurate graphs for the population amplitudes; representing in figure B2. The prominent element to note is the very slow variation of the population amplitude d_0 with increasing κ, amazingly adjusting with the numerical solutions, a few of which represent in figure 8 of the text.

Indeed, these last elements constitute extra developments that are not essential in the comprehension of the Lorenz dynamics, describing in terms of our autonomous oscillator. Nonetheless, they bring some quite valuable information to the 3D features, which do not transpire from the original set.

Appendix C

C.1. High-order field and population components: general expressions

A general expression for the electric field component is

$$e_{2n+1}(t) = E_{2n+1}\cos((2n+1)\omega t), \quad \text{(C1}a\text{)}$$

from which deduce

$$\dot{e}_{2n+1}(t) = -(2n+1)\omega E_{2n+1}\sin((2n+1)\omega t), \quad \text{(C1}b\text{)}$$

$$e_{2n+1}^2(t) = E_{2n+1}^2(t)\cos^2((2n+1)\omega t)) = E_{2n+1}^2\frac{1+\cos(2(2n+1)\omega t)}{2}, \quad \text{(C1}c\text{)}$$

$$e_{2n+1}(t)\dot{e}_{2n+1}(t) = -(2n+1)\omega E_1^2\sin((2n+1)\omega t) \times\cos((2n+1)\omega t) = -\frac{2n+1}{2}\omega E_1^2\sin(2(2n+1)\omega t), \quad \text{(C1}d\text{)}$$

$$\dot{e}_{2n+1}^2(t) = (2n+1)^2\omega^2 E_{2n+1}^2\sin^2((2n+1)\omega t) = (2n+1)^2\omega^2 E_{2n+1}^2\frac{1-\cos(2(2n+1)\omega t)}{2}. \quad \text{(C1}e\text{)}$$

These developments gather into equation (3) to yield

$$\frac{1}{\gamma}\ddot{D}(t) + \dot{D}(t) + E_{2n+1}^2\frac{1+\cos(2(2n+1)\omega t)}{2}D(t) = \frac{1}{2C}\frac{E_{2n+1}^2}{2}\left\{\left(\frac{(2n+1)^2\omega^2}{\kappa}-1\right) - (2n+1)\omega\left(1-\frac{1}{\kappa}\right)\right\} \times\sin(2(2n+1)\omega t) - \left(1+\frac{(2n+1)^2\omega^2}{\kappa}\right)\cos(2(2n+1)\omega t)\Bigg\} \quad \text{(C2)}$$

The driving left-hand expression contains exclusive even harmonics,

$$f_{2n}(t) = f_{2n}^{0} + f_{2n}^{1}\cos(2n\omega t) + f_{2n}^{2}\sin(2n\omega t) \qquad \text{(C3)}$$

imposing the population nth-order response to develop accordingly

$$D_{2n}(t) = D_{2n}^{0} + D_{2n}^{1}\cos(2n\omega t) + D_{2n}^{2}\sin(2n\omega t) \qquad \text{(C4)}$$

Carrying out the algebra, a general formula for the phase-lag expression between high-order field and population components derives as

$$\tan(\varphi_n) = \frac{D_{2n+1}^{2}}{D_{2n+1}^{1}} = \frac{(\kappa-1)\left[-\dfrac{4(2n+1)^2\omega^2}{\gamma} + \dfrac{E_{2n+1}^{2}}{2}\right] + 2(2n+1)\omega^2}{\left\{-\dfrac{4(2n+1)^2\omega^2}{\gamma} + \dfrac{E_{2n+1}^{2}}{2} - 2(2n+1)(-1)\right\}\omega} \qquad \text{(C5)}$$

Yielding, for the third order, in field amplitude

$$\tan(\varphi_3) = \frac{D_3^2}{D_3^1} \cong (\kappa-1)\sqrt{\frac{(\kappa-2)(\kappa+1)}{2\kappa}} \times \frac{60\kappa}{72\kappa(\kappa+1) + 6(\kappa-2)(\kappa-1)} \qquad \text{(C6)}$$

We leave it as a simple exercise, using any graphical software, to verify the perfect match between this last expression and equation (19*b*). An additional indication of the oscillator cogency. The fact that the same phase value obtains with the first and third order harmonic of the electric field is quite satisfactory. This only means that any electric field harmonic carries the same time lag with its corresponding population order. $E_1\cos(\omega t)$ with $d_0\cos(\omega t - \varphi_1)$ and $E_3\cos(3\omega t)$ with $D_3\cos(2\times 3\omega t - \varphi_3)$, and so on.

However, let us note that in order to retrieve the population 4th order harmonic, for example, one has to solve the oscillator equation imposing an electric field of the form $E(t) = E_1\cos(\omega t) + E_3\cos(3\omega t)$. Sa that $E(t)^2 = (E_1\cos(\omega t) + E_3\cos(3\omega t))^2$ transforms into

$$E(t)^2 = \frac{E_1^2}{2}(1 + \cos(2\omega t)) + \frac{E_3^2}{2}(1 + \cos(6\omega t)) + E_1E_3(\cos(4\omega t) + \cos(2\omega t)) \qquad \text{(C7}a\text{)}$$

i.e.

$$E(t)^2 = \frac{E_1^2}{2} + \frac{E_3^2}{2} + \left(\frac{E_1^2}{2} + E_1E_3\right)\cos(2\omega t) + E_1E_3\cos(4\omega t) + \frac{E_3^2}{2}\cos(6\omega t) \qquad \text{(C7}b\text{)}$$

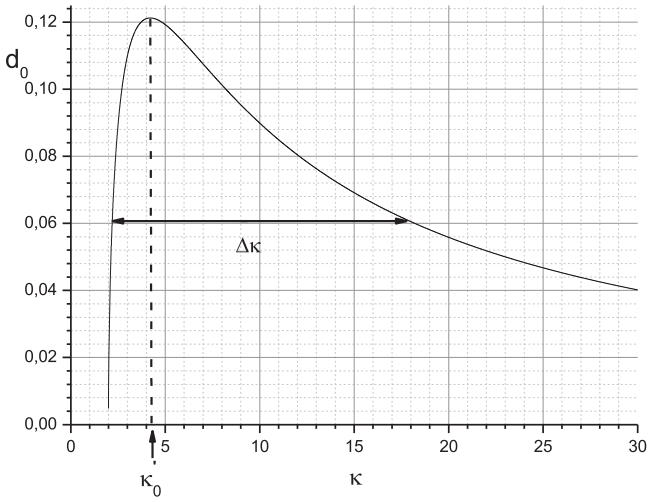

Figure C1. Resonant response to a perturbing electric field $e\cos(\omega t)$, describing the population amplitude d_0 with respect to the cavity decay rate κ.

The importance of beat notes between the first and third order field components transpires clearly in this last development. A far-reaching analysis should consider such beat-notes.

However, doing so will only bring minor quantitative improvements with respect to population amplitudes, not adding any qualitative features to the oscillator characteristics.

Appendix D

D.1. What about chaos?

The fascination the Lorenz equations carried, for more than half a century, being due to the well-known deterministic chaos they deliver for typical control parameter values; one would be quite right to ask how the oscillator model may provide some clues with respect to the inextricable solutions that signature the strange attractor. Indeed, reducing the 3D model to a second order differential equation confers the system some permanency that handles the periodic attractors, provided harmonic solution impose to the electric field, but the single equation cannot depict any complicated aperiodicity such as the erratic signals that shape the strange attractor. However, the oscillator model delimits astonishingly well the region, i.e. the bandwidth for chaotic solutions with respect to the lone control parameter κ. For thru clarifications, let us represent again the population-oscillation amplitude $d_0(\kappa)$ (figure 6) in figure C1.

Quantitative elements summarize as follows. The amplitude is half its maximum value for $\kappa_m = 2.2$ and $\kappa_M = 17.9$. While, numerical analyses show a region of full chaos extending from $\kappa_m = 2.21$ to $\kappa_M = 16.7$ [13]. From such an almost similar realm of values, one entitles to conclude that the population half-maximum bandwidth corresponds to the region of unpredictably non-periodic solutions, i.e. that of deterministic chaos.

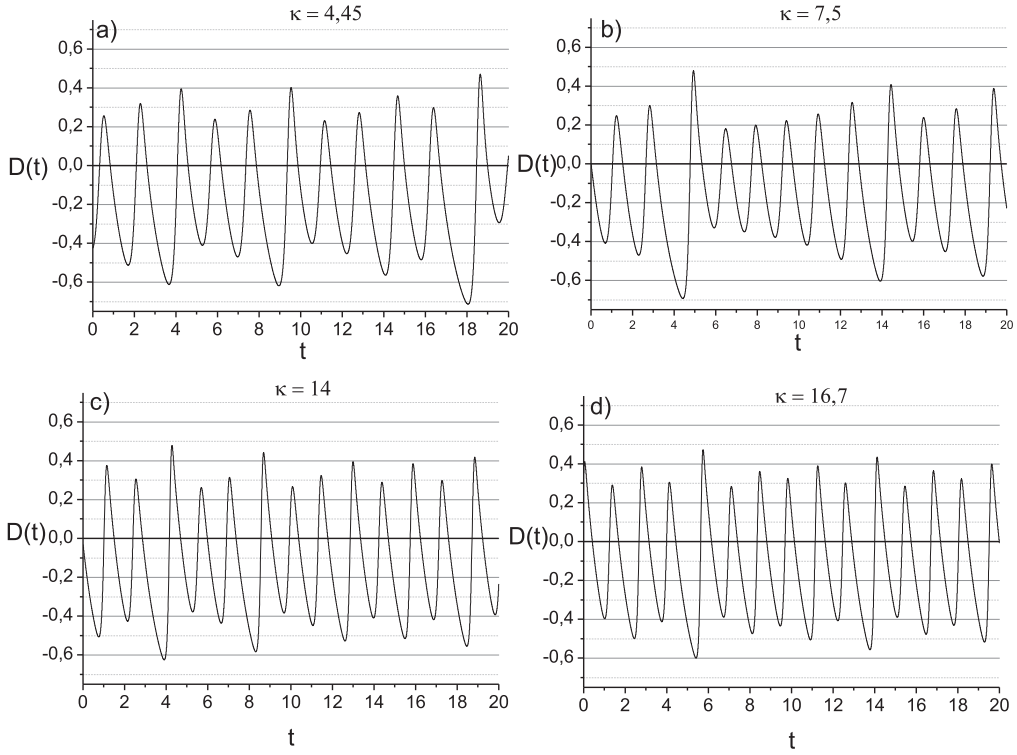

Figure C2. Population signals obtained inside the chaotic region for (a) $\kappa = 4.45$, (b) $\kappa = 7.5$, (c) $\kappa = 14$, and (d) $\kappa = 16.7$.

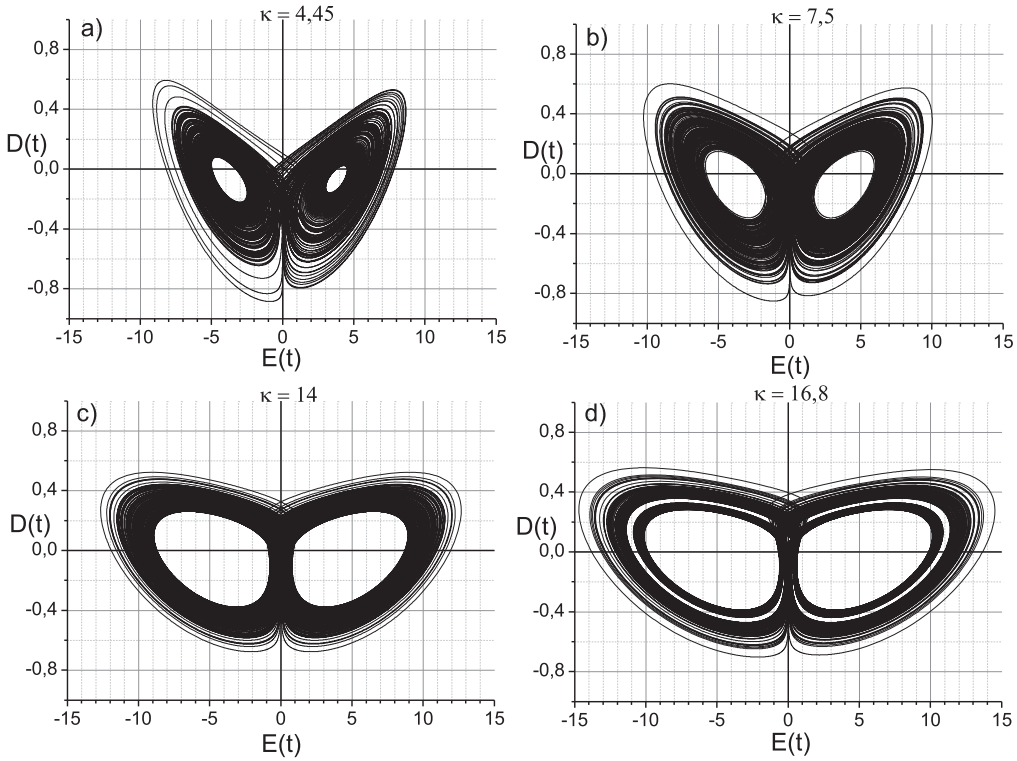

Figur C3. Strange attractor shaping with increasing cavity decay rate; (a) $\kappa = 4.45$, (b) $\kappa = 7.5$, (c) $\kappa = 14$, and (d) $\kappa = 16.7$.

A few examples of the population inversion time trace, obtained with a series of κ values embedded inside the bandwidth for resonance represent in figure C2. All signals undergo irregular oscillations between a minimum lower limit $d_m \cong -0.7$ and a positive peak value $d_M \cong 0.5$.

For better resolution, the above figures limit to a time span $\Delta t = 20$. Phase space representations, figure C3, allow for larger extensions of the signals duration and further information with respect to the population amplitude. During its development, amplitude may attain lower values,

extending down to $d_m \cong -0.9$, for the negative limit and $d_M \cong 0.6$, for the positive one. These limits mainly characterize the upper zone of the resonant curve, as in the examples of figures C3(a) and (b).

Note the change in contour-shaping with respect to κ. For κ close to the characteristic value κ_0(at resonance), the strange attractor is asymmetric, as in figures C3(a) and (b). Increasing κ, turns the orbit into symmetric, before being forced to evolve along the S1 trajectory of figure 12(d), after a few cascading of the higher-order type.

As for modelling these chaotic solutions, such a task goes well beyond the simple oscillator model studied herein. Yet, a few hints recently put forward to do so [13].

Appendix E

E.1. The forced mass-spring and other typical oscillators

The easiest way to capture the resonant features and other properties of the non-linear laser oscillator is to recall the main characteristics of the externally driven one-dimensional mass-spring system, represented in figure E1.

Submitted to some sinusoidal force $f(t) = f_0 \cos(\omega t)$ at the opposite end of the spring, the mass oscillates on a horizontal support with some viscous friction α. Its movement obeys a second order differential equation of the form

$$\ddot{x} + 2\alpha\dot{x} + \omega_0^2 x = a\cos(\omega t) \tag{E1}$$

Where ω_0 is the system's proper-pulsation-frequency. It relates to the mass and to some characteristic constant k -which puts a figure on the spring elasticity- through $\omega_0 = \sqrt{\frac{k}{m}}$.

The solution to equation (E1) writes

$$x(t) = A\cos(\omega t) + B\sin(\omega t) \tag{E2}$$

Straightforward manipulations and algebra yield

$$A(\omega) = \frac{\omega_0^2 - \omega^2}{(\omega_0^2 - \omega^2)^2 + (2\alpha)^2\omega^2}a = \frac{1 - \frac{\omega^2}{\omega_0^2}}{\left(1 - \frac{\omega^2}{\omega_0^2}\right)^2 + \left(\frac{2\alpha}{\omega_0}\right)^2\frac{\omega^2}{\omega_0^2}}\frac{a}{\omega_0^2} \tag{E3a}$$

$$B(\omega) = \frac{2\alpha\omega}{(\omega_0^2 - \omega^2)^2 + (2\alpha)^2\omega^2}a = \frac{\frac{2\alpha}{\omega_0}\frac{\omega}{\omega_0}}{\left(1 - \frac{\omega^2}{\omega_0^2}\right)^2 + \left(\frac{2\alpha}{\omega_0}\right)^2\frac{\omega^2}{\omega_0^2}}\frac{a}{\omega_0^2} \tag{E3b}$$

Figure E1. Schematic representation of a forced mass-spring oscillator placed on a horizontal plane. Some harmonic force acts at one end of a spring to impose its rhythm to a mass m at the other end.

The oscillator characteristics obtain transforming $A\cos(\omega t) + B\sin(\omega t)$ into $C\cos(\omega t - \varphi)$, with

$$C = \sqrt{A^2 + B^2} = \frac{a}{\sqrt{(\omega_0^2 - \omega^2)^2 + (2\alpha)^2\omega^2}} \tag{E4a}$$

$$\tan(\varphi) = \frac{B}{A} = \frac{2\alpha\omega}{\omega_0^2 - \omega^2} \tag{E4b}$$

Maximum and minimum amplitudes evaluate setting equation (E4*a*) derivative equal to zero

$$\frac{dC}{d\omega} = a\frac{2\omega(\omega_0^2 - \omega^2 - 2\alpha^2)}{((\omega_0^2 - \omega^2)^2 + (2\alpha)^2\omega^2)^{3/2}} = 0, \tag{E5}$$

The solutions, $\omega = 0$ and $\omega = \sqrt{\omega_0^2 - 2\alpha^2}$, yield minimum and maximum amplitudes $C_m = \frac{a}{\omega_0^2}$ and $C_M = \frac{a}{2\alpha\omega_0\sqrt{1 - \left(\frac{\alpha}{\omega_0}\right)^2}}$, with $C_M \cong \frac{a}{2\alpha\omega_0}$ for low damping ($\alpha \ll \omega_0$).

E.2. Bandwidth for resonance and phase delay with respect to the external excitation

As in electric circuits, frequency bandwidth is the frequency domain for which the amplitude evolves from C_M to $\frac{C_M}{\sqrt{2}}$ (energy evaluating at half its maximum value). The bandwidth frequency-limits ω_1 and ω_2 obtain setting $C(\omega) = \frac{C_M}{\sqrt{2}}$, i.e.

$$\frac{a}{\sqrt{(\omega_0^2 - \omega^2)^2 + (2\alpha)^2\omega^2}} = \frac{1}{\sqrt{2}}\frac{a}{2\alpha\omega_0} \tag{E6a}$$

From which we extract

$$\omega_\pm = \omega_0\sqrt{1 \pm \frac{2\alpha}{\omega_0}} \cong \omega_0 \pm \alpha \tag{E6b}$$

And a frequency pulsation bandwidth $\Delta\omega = \omega_+ - \omega_- \cong 2\alpha$.

E.3. Resonance and phase depictions with normalized quantities

For forthright graphical representations, amplitude and phase rewrite in terms of the normalized pulsation $\frac{\omega}{\omega_0}$

$$C\left(\frac{\omega}{\omega_0}\right) = \frac{a}{\omega_0^2\sqrt{\left(1 - \frac{\omega^2}{\omega_0^2}\right)^2 + \left(\frac{2\alpha}{\omega_0}\right)^2\frac{\omega^2}{\omega_0^2}}} \tag{E7a}$$

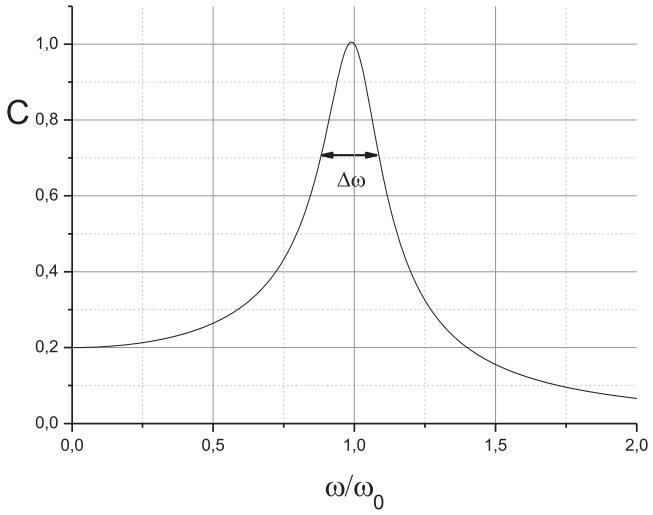

Figure E2. Resonant characteristics of the forced mass-spring oscillator as a function of the normalized pulsation $\frac{\omega}{\omega_0}$.

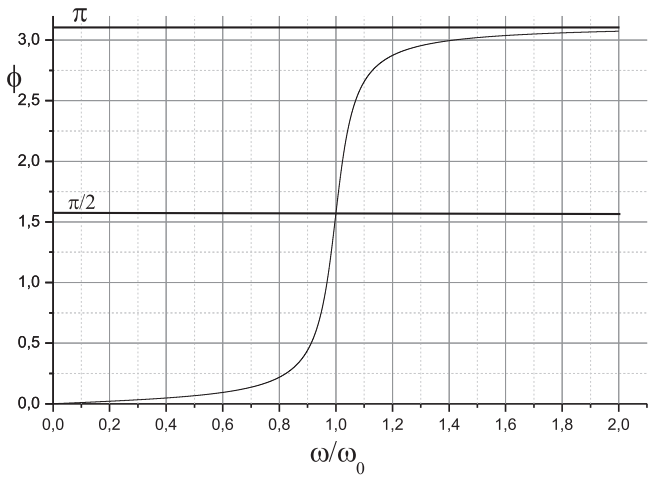

Figure E3. Phase difference between the exciting force and the oscillator response as a function of the normalized pulsation $\frac{\omega}{\omega_0}$.

$$\tan(\varphi) = \frac{2\alpha}{\omega_0}\frac{\omega}{\omega_0}\left(\frac{1}{1-\frac{\omega^2}{\omega_0^2}}\right) \tag{E7b}$$

With $\frac{\alpha}{\omega_0} = 0.1$, and $a = 1$, we obtain figure E2, for $C\left(\frac{\omega}{\omega_0}\right)$, and figure E3, for $\varphi\left(\frac{\omega}{\omega_0}\right)$.

The resonant and phase curves indicate that for low frequencies, the mass response is linear with respect to the external force, the mass position phase locking with the external excitation.

The amplitude and phase increase with frequency, up to a maximum amplitude, occurring at the system's characteristic $f_0 = \frac{\omega_0}{2\pi}$ and a phase reaching $\frac{\pi}{2}$, at which point $A(\omega_0) = 0$ and $B(\omega_0) = C_M = \frac{a}{2\alpha\omega_0}$. The mass position tracking as

$$x(t) = \frac{a}{2\alpha\omega_0}\sin(\omega_0 t), \tag{E8}$$

i.e. with a phase quadrature with respect the external excitation. Away from ω_0, the amplitude decreases towards asymptotic values $C(\omega) = \frac{a}{\omega^2}$, whereas the phase continues to increase towards its maximum value π, imposing a mass movement of the form

$$x(t) = -\frac{a}{\omega^2}\cos(\omega t) \tag{E9}$$

i.e. in total phase-opposition with the driving excitation.

Most of the described mass-spring resonant and phase delay properties characterize the self-sustained Lorenz-Haken oscillator, as fully demonstrated in the text and additional substance in the appendixes.

As an ultimate proof to the fact that the field-population oscillator and the mass-spring system have much in common, let us follow the instantaneous position $x(t)$ as a function of the driving force; the external pulsation ω as a unique control parameter.

In the limit of small ω's, the mass position and driving force follow the straight line of figure E4(a); $x(t)$ softly submitting to the external force, with no phase difference. Any pulsation increase transforms the trajectory into an ellipse, with the previous straight line as the principal axis. Higher ω values make the orbit swell, due to the phase growth, in accordance to figure E3 and equation (E7*b*), before orbiting a closed loop with maximum perimeter, at $\omega = \omega_0$ and $\varphi = \frac{\pi}{2}$, reorienting gradually to end up again in a straight line perpendicular to that of figure E4(a).

Phase space trajectories model through

$$x_A(t) = a\cos(\omega t) \tag{E10a}$$

quantifying the movement of the spring extremity A, undergoing the external force, and

$$x(t) = C(\omega)\cos(\omega t - \varphi) = C(\omega)\cos(\omega t)\cos(\varphi) + C(\omega)\sin(\omega t)\sin(\varphi) \tag{E10b}$$

describing the mass movement.

The two equations assemble in the general contour of an ellipse

$$\left(\frac{x(t)}{C(\omega)}\right)^2 + \left(\frac{x_A(t)}{a}\right)^2\cos^2(\varphi) - 2\frac{x(t)}{C(\omega)}\frac{x_A(t)}{a} \times \cos(\varphi) = \sin^2(\varphi) \tag{E11}$$

for any phase value not equal to the typical values 0 and π.

For $\varphi = 0$, the system describes the straight-line of figure E4(a) following

$$x(t) = \frac{a}{\omega_0^2}x_A(t) \tag{E12}$$

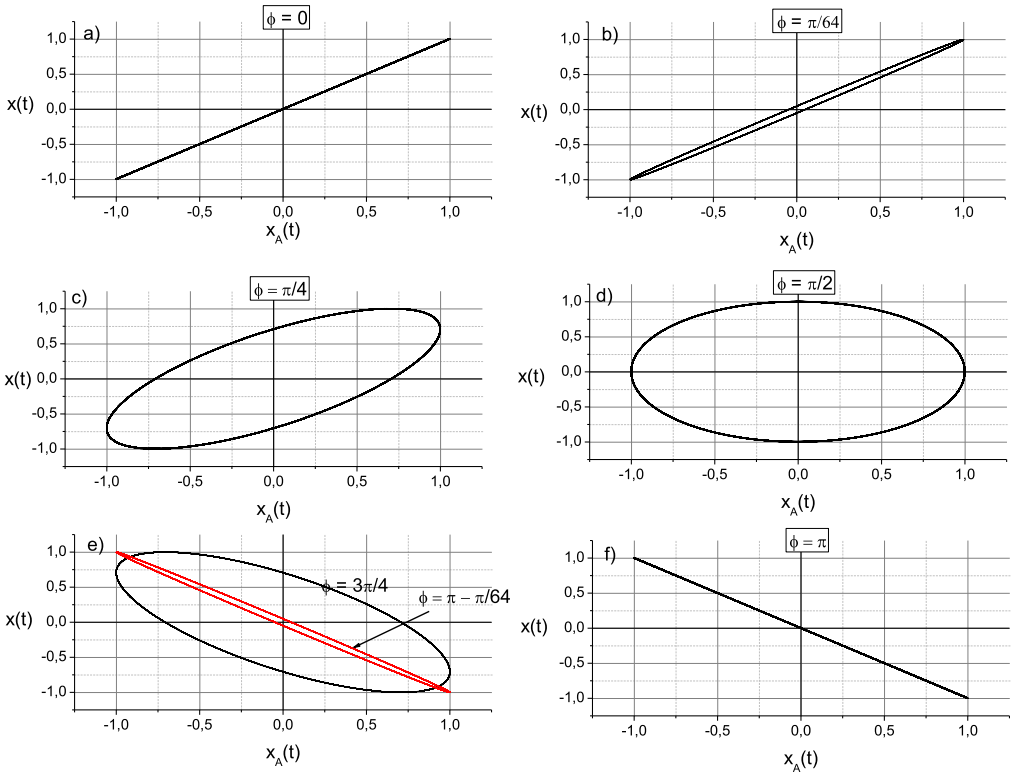

Figure E4. Phase space orbits representing the mass position with respect to the spring end A submitted to some harmonic excitation. Phase varies from (a) $\varphi = 0$, (b) $\varphi = \pi/64$, (c) $\varphi = \pi/4$, (d) $\varphi = \pi/2$, (e) $\varphi = 3\pi/4$ and $\varphi = \pi - \pi/64$, to (f) $\varphi = \pi$.

For $\varphi = \pi$, the straight line reorients to follow (figure E4(f))

$$x(t) = -\frac{a}{\omega_0^2} x_A(t) \tag{E13}$$

Between these two extreme values, a series of inclined ellipses at the left and right sides of the symmetric one, which relates to $\varphi = \frac{\pi}{2}$ (figure E4(d)): figure E4(b) associates to $\varphi = \frac{\pi}{64}$, figure E4(c) to $\varphi = \frac{\pi}{4}$, figure E4(e) to $\varphi = \frac{3\pi}{4}$ and $\varphi = \pi - \frac{\pi}{64}$.

Comparisons between figure E4 orbits and the trajectories of figures 2 and 3 in the text persuasively acknowledge the compelling transformation of the Lorenz-Haken equations into a nonlinear oscillator, out of which much of the phase dependent dynamics pulls-out. The light-matter dynamics embedded in the nonlinear oscillator appears as the result of resonant effects described in terms of the population response to the electric field, as conforming to the cavity decay-rate value κ, the system's lone control parameter.

Experimentally, instantaneous representations of the phase space portraits depicted in figure E4 need some adapted devices to monitor the movement of mass m as a function of the position of the spring other-extremity. The required test bench should not be easy to realize.

A simpler experiment is that of an equivalent electrical RLC circuit, as that of figure E5. Submitted to a sinusoidal electric potential $v(t) = v_0 \cos(\omega t)$, the current $i(t)$ circulating in the circuit obeys the same differential equation as

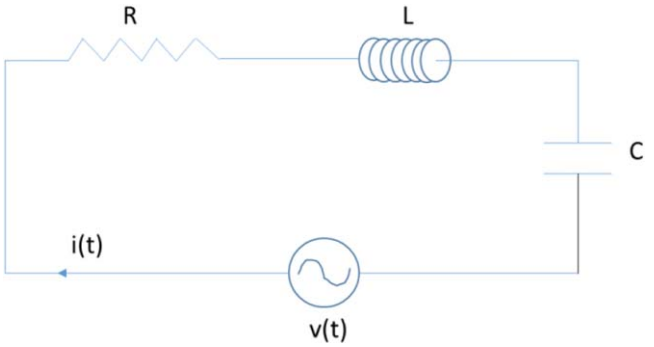

Figure E5. RLC circuit excited with a sinusoidal potential v(t). The current response i(t) follows the same resonant properties as those of a mass-spring system.

equation (E1), writing in terms of the electrical elements

$$\frac{d^2 i}{dt^2} + \frac{R}{L}\frac{di}{dt} + \frac{1}{LC} i = i_0 \cos(\omega t) \tag{E14}$$

It should only take a double-entry oscilloscope, monitoring the excitation and circuit response, to reproduce any orbit in phase space.

Another similarity, in terms of phase-space trajectories, pulls out from basic optics and electromagnetism. Those familiar with electric field reorientation occurring when a linearly polarized beam of light crosses some birefringent material, surely recognize the descriptive elements of light polarization, which may rapidly summarize with normalized quantities. Consider an x and y component of some linearly polarized field propagating along some z-axis (figure E6).

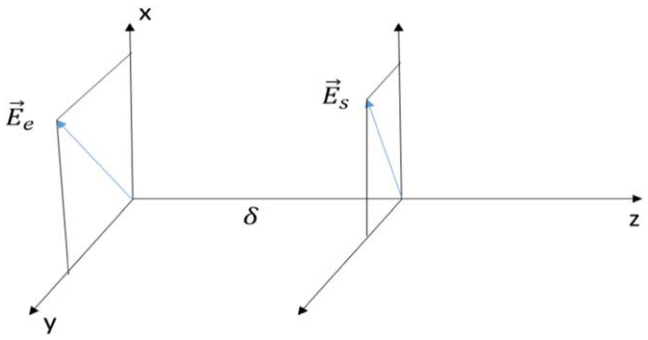

Figure E6. Incident wave on a birefringent medium of thickness δ. The output wave polarization relates to δ and to the birefringence $n_x - n_y$.

When, at the entrance of a birefringent slab of thickness δ, some linearly field decomposes its E_x and E_y components, these emerge from the slab with some phase difference $\varphi = 2\pi\frac{\delta}{\lambda}$, where λ is the electric field wavelength, considered monochromatic. The two components describe as $E_x = E_{0x}\cos(\omega t)$ and $E_y = E_{0y}\cos(\omega t - \varphi)$, transforming into the same expression as equation (E11).

An adequate variable change $X = \frac{E_x}{E_{0x}}$ and $Y = \frac{E_y}{E_{0y}}$ yield the normalized general form for an elliptical-polarization description

$$X^2 + Y^2 - 2XY\cos(\varphi) = \sin^2(\varphi) \qquad \text{(E15)}$$

Where $\varphi = 2\pi\frac{\delta}{\lambda}$.

We immediately identify the linearly polarized output $Y = X$, typical of a multiple wavelength slab of thickness δ, for which $\delta = n\lambda$; that of a half-wavelength slab $Y = -X$, for which $\delta = (2n+1)\frac{\lambda}{2}$; and that of quarter-wavelength, with $\delta = (2n+1)\frac{\lambda}{4}$, which transforms linear into circularly polarized light, rotating along the symmetric trajectory $X^2 + Y^2 = 1$, when the electric field hits the slab at 45° of the birefringent-material proper-axes, x and y.

ORCID iDs

Belkacem Meziane https://orcid.org/0000-0002-8554-6904

References

[1] Lorenz E N 1963 Deterministic nonperiodic flow *J. Atmos. Sci.* **20** 130
[2] Haken H 1975 Analogy between higher instabilities in fluids and lasers *Phys. Lett.* A **53** 77
[3] Van Tartwijk G H M and Agrawal G P 1997 Nonlinear dynamics in the generalized Lorenz-Haken model *Opt. Commun.* **133** 565–77
[4] Galias Z and Zgliczy´nski P 1998 Computer assisted proof of chaos in the Lorenz equations *Physica* D **115** 165–88
[5] Smale S 1998 Mathematical problems for the next century *Math. Intell.* **20** 7–15
[6] Lakshmivaraha S, Baldwin M E and Zheng T 2006 Further Analysis of Lorenz's Maximum Simplification Equations *J. Atmos. Sci.* **63** 2673–99
[7] Meziane B 2009 Pulse structuring in laser-light dynamics: from weak to strong sideband analyses: II – the Lorenz-Haken model *Atomic, Molecular and Optical Physics: New Research* ed L T Chen (New York: Nova Science Publishers) ch II pp 61–107
[8] Tucker W 2002 A rigorous ODE solver and smale's 14th problem *Found. Comput. Math.* **2** 53–117
[9] Mello L F, Messias M and Braga D C 2008 Bifurcation analysis of a new Lorenz-like chaotic system *Chaos, Solitons Fractals* **37** 1244–55
[10] Dullin H R *et al* 2007 Extended phase diagram of the Lorenz model *Int. J. Bifurcation Chaos* **17** 3013–33
[11] Zhou T S *et al* 2004 The complicated trajectory behaviours in the Lorenz equation *Chaos Solitons Fractals* **19** 863–73
[12] Meziane B 2016 Isomorphic transformation of the Lorenz equations into a single-control-parameter structure Int *J. Eng. Res. Sci.* **2** 70–8
[13] Meziane B 2019 Lorenz-Haken dynamics-analytical framework: from symmetric to asymmetric trajectories *Phys. Scr.* **94** 125217